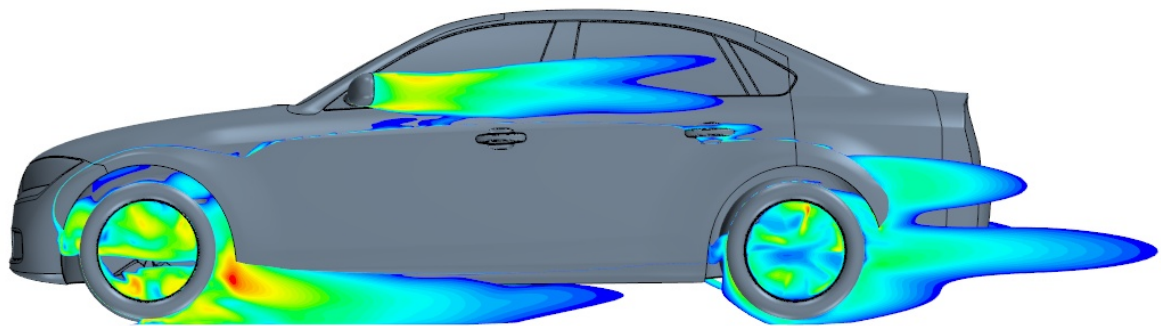




CHALMERS



Aeroacoustic sound sources around the wheels of a passenger car

A Computational Fluid Dynamics study using steady state models to evaluate main sources of flow noise

Master's thesis in Applied Mechanics

EMIL RINGWALL

MASTER'S THESIS IN APPLIED MECHANICS

Aeroacoustic sound sources around the wheels of a passenger car

A Computational Fluid Dynamics study using steady state models to evaluate main sources of flow noise

EMIL RINGWALL

Department of Applied Mechanics
Division of Vehicle Engineering and Autonomous Systems
CHALMERS UNIVERSITY OF TECHNOLOGY

Göteborg, Sweden 2017

Aeroacoustic sound sources around the wheels of a passenger car
A Computational Fluid Dynamics study using steady state models to evaluate main sources of flow noise
EMIL RINGWALL

© EMIL RINGWALL, 2017

Master's thesis 2017:67
ISSN 1652-8557
Department of Applied Mechanics
Division of Vehicle Engineering and Autonomous Systems
Chalmers University of Technology
SE-412 96 Göteborg
Sweden
Telephone: +46 (0)31-772 1000

Cover:
Illustration of Proudman sound sources around the wheels and rear view mirror of the DrivAer model.

Chalmers Reproservice
Göteborg, Sweden 2017

Aeroacoustic sound sources around the wheels of a passenger car
A Computational Fluid Dynamics study using steady state models to evaluate main sources of flow noise
Master's thesis in Applied Mechanics
EMIL RINGWALL
Department of Applied Mechanics
Division of Vehicle Engineering and Autonomous Systems
Chalmers University of Technology

ABSTRACT

When speaking about wheel noise most people think about the contact noise from wheel and road interaction. Previous experimental studies in wind tunnels show there is an apparent aerodynamic noise source near the front wheels. New legislative demands force car manufacturers to reduce the noise emitted and the wheel noise cannot be ignored anymore.

The study has used broadband noise source models incorporated into the commercial software Star CCM+ to locate and analyze sources generated by dipoles and quadrupoles within the flow around the wheels of a DrivAer car model. The methods used are the Curle acoustic analogy, to approximate the dipole sources at the surface, Proudman acoustic analogy, to approximate the quadrupoles generated in the turbulent flow and the Lilley method, approximates the turbulent shear flow sources.

Four cases have been studied comparing stationary and rotating wheels as well as open and closed rims. All cases studied show significant sources of noise at the front wheels and the simulations have shown a clear dependence of both rim geometry and rotation of the wheels. It is shown that wheel rotation gives a significant increase in aeroacoustic noise in both dipole and quadrupole sources while geometry dependence only could be noted in the quadrupole sources.

Keywords: CFD, CAA, aeroacoustics, DrivAer, wheel noise, Star CCM+, Steady-State, CTH, Chalmers

PREFACE

This project was carried out at the Department of Applied Mechanics, Vehicle Engineering and Autonomous Systems, Chalmers University of Technology during the winter of 2016/2017 and presented in June 2017. The thesis was the final step towards the Master of Science in Engineering degree and contains the final results of the studies. The simulations were performed on resources provided by the Swedish National Infrastructure for Computing (SNIC) at Chalmers Centre for Computational Science and Engineering (C3SE).

Many thanks to my supervisor Ph.D. Olga Roditcheva and my examiner Associate Professor Simone Sebben for all support and trust in my independent work. I would like to send a special thanks to Ph.D student Emil Ljungskog for all his support in Star CCM+ and Linux related questions.

Finally, I would like to thank my family for all the help while finalizing the report and especially my girlfriend and daughters for all the love and belief in me.

Emil Ringwall, Gothenburg, June 2017

Nomenclature

Greek

δ_{ij}	dirac delta
μ	dynamic viscosity
ρ	density
σ	stress
ε	dissipation

Latin

\mathbf{n}	Surface unit normal vector
\mathbf{x}	location of noise source
\mathbf{y}	location of spectator
a	speed of sound
C_d	drag coefficient
C_p	specific heat, constant pressure
C_v	specific heat, constant volume
$dB(A)$	A-weighted Decibel
f_V	external volume force
I	Intensity
k	turbulent kinetic energy
L	turbulent length scale
l	characteristic length scale
L_{den}	Day-evening-night level
m	mass
p	pressure
P_i	surface distribution of dipoles
Re	Reynolds number
T	turbulent time scale
t	time
T_{ij}	Lighthill stress tensor
U	mean velocity
u	velocity
y^+	non-dimensional wall distance

Subscripts

0	ambient
i, j, k	indices
ref	reference value
rms	root mean square
S	surface
V	volume

Superscripts

' Fluctuation

Acronyms

<i>AP</i>	Acoustic Power
<i>C3SE</i>	Chalmers Center for Computational Science and Engineering
<i>CAA</i>	Computational Aeroacoustics
<i>CAD</i>	Computer Aided Design
<i>CFD</i>	Computational Fluid Dynamics
<i>CPU</i>	Central Processing Unit
<i>DNS</i>	Direct Numerical Simulations
<i>EU</i>	European Union
<i>MRF</i>	Moving Reference Frame
<i>PAP</i>	Proudman Acoustic Power
<i>RANS</i>	Reynolds Averaged Navier Stokes
<i>SAP</i>	Surface Acoustic Power (Curle)
<i>SNGR</i>	Stochastic Noise Generation and Radiation
<i>SNIC</i>	Swedish National Infrastructure for Computing
<i>TKE</i>	Turbulent Kinetic Energy
<i>WHO</i>	World Health Organization

CONTENTS

Abstract	i
Preface	iii
Nomenclature	v
Contents	vii
1 Introduction	1
1.1 Background	1
1.2 Aim	1
1.3 Scope	2
2 Theory	3
2.1 Fluid Dynamics	3
2.1.1 Turbulence	3
2.1.2 Computational Fluid Dynamics	3
2.1.2.1 Reynolds Averaged Navier Stokes	3
2.2 Acoustics	4
2.2.1 Aeroacoustics	4
2.2.1.1 Lighthill Acoustic Analogy	4
2.2.1.2 Acoustic sources	5
2.2.1.3 Broadband Noise Source Models	5
2.2.1.4 Curle noise source model	5
2.2.1.5 Proudman noise source model	6
2.2.1.6 Lilley noise source model	6
3 Methodology	8
3.1 Geometry preparation	8
3.1.1 Car Geometry	8
3.1.2 Computational domain	9
3.2 Case setup	10
3.2.1 Mesh generation	10
3.2.2 Physics setup	12
3.3 Simulation	13
3.4 Post-processing	13
4 Results and Discussion	14
4.1 Flow characteristics	14
4.1.1 Pressure	14
4.1.2 Velocity	15
4.1.2.1 Velocity magnitude at $z = 0.5$ m	16
4.1.2.2 Velocity magnitude at $z = 0.34$ m	18
4.1.2.3 Velocity magnitude at $z = 0.16$ m	20
4.2 Acoustic sound sources	22
4.2.1 Curle Noise Source Model	22
4.2.2 Proudman Noise Source Model	24
4.2.2.1 Proudman Acoustic Power compared to Turbulent Kinetic Energy	28
4.2.3 Lilley Noise Source Model	30
5 Conclusions	32
5.1 Future work	32
References	33

1 Introduction

In this thesis, sound induced by the flow around the wheels of a passenger car is simulated. A total of four cases are simulated to identify sound sources around the wheels of a DrivAer car. The goal is to identify the influence from the rotation of the wheels as well as the difference between five spoke rims and completely closed ones, with regard to dipole and quadrupole sound sources.

1.1 Background

The view of noise in or from a car hasn't always been as it is today. For a long time, a loud engine expressed power and a fast car. Today, cars are widely used for commuting and long business trips and therefore a higher demand is on comfort. Too much noise is shown to cause tiredness, headaches, irritation etc and even if much is done to reduce known sources new ones always appear. Today the focus is mainly to improve the environment for the customers inside the cars. But, there is a world outside.

In the European Union (EU) noise policy, it is stated that "65% of Europeans living in major urban areas are exposed to high noise levels" which is more than 55 dB L_{den} (day-evening-night level), and the main part of that noise comes from transportation [1]. At the same time World Health Organization (WHO) reports that, environmental noise causes 43 000 hospital admissions and 10 000 cases of premature deaths related to coronary heart disease every year. In addition, not only humans are affected by environmental noise. Recent research shows harmful effects on wildlife as well. Many animals rely on acoustic communication for e.g. mating or finding food [2].

The first European regulation of noise emitted by passenger cars came in 1970 and allowed a maximum of 82 dB(A) 7.5 m from the centerline of the car. Revisions have been made regularly and by today the limit is 72 dB(A) and by 2026 it will be 68 dB(A) [3]. Still that is far from the 55 dB L_{den} recommendations made by WHO. The main focus in the EU is directed to measure the environmental noise within urbanized areas, where most people live, even if heavy traffic in rural areas can disturb the wildlife significantly. Therefore it is necessary to consider noise that only appear at high velocities as well.

Today, most of the research on noise is directed to the driver experience and noise reduction inside the car. For instance, a lot of studies have been done regarding the rear-view mirrors and the beams next to the windshield (A-pillar) which both give a major contribution to the noise in the cabin. Regarding the wheels a lot of research has been done concerning road noise and aerodynamics. Road noise being the sound originating from the contact between the tire and ground. It has also been known for a long time that there is a major sound source, generated by the flow, near the front wheels but as it is not affecting the cabin due to the firewall the interest has been low [4]. Additionally, there has been a problem to study the contribution from wheel rotation as the mechanisms rotating the wheels in the wind tunnels give too much background noise to give reliable results.

Analytical aeroacoustics is a relatively new field of study, which originated in the early 1950's from the aircraft segment as the noise from the jet engine became of interest to researchers. Due to the limited use of computational analysis historically, most of the acoustic research has been and still is performed in a wind tunnel. Leading German manufacturers are in the process of building or have recently built wind tunnels designed for aeroacoustic testing. Computational aeroacoustics (CAA) has recently grown into a usable method as computer power and software have reached a state where it is possible to make simulations at a sufficient mesh quality.

1.2 Aim

The aim of the study is to numerically identify the intensity and location of the main sound sources induced by the aerodynamic flow around the wheels of a DrivAer car model. A comparison is made between stationary and rotating wheels as well as between closed and open rims, using the Computational Fluid Dynamics (CFD) software Star CCM+. Four different simulations are run in a 2-equation steady state Reynolds Averages Navier-Stokes (RANS), which is required for the noise source models Curle and Proudman. Additionally, all four cases are after convergence run with a specific Lilley solver using the Stochastic Noise Generation and Radiation (SNGR) model, which compute a synthetic turbulence field, to visualize the noise from turbulent shear flow. The Curle model is used to evaluate the acoustic power per unit surface originating from the

interaction of a turbulent boundary layer with a solid body and the Proudman model evaluates acoustic power per unit volume generated by quadrupole sound sources generated by isotropic turbulence.

1.3 Scope

This study is limited to numerical simulations only. Therefore, the presented numerical values are to be considered as approximate values. All cases have been set up with the intention to be as identical as possible, regarding geometry and other settings. The research intend to investigate the aerodynamic properties in order to understand the underlying influence they have on the aeroacoustic properties studied.

2 Theory

A brief explanation of the underlying theory for this report with the focus on aeroacoustics is given here.

2.1 Fluid Dynamics

The study of fluids in motion dates back to the time of Archimedes, and probably even earlier. But it was not until the 19th century the governing equations known today was developed by Navier and Stokes [5]. The equations for an arbitrary flow are given by Equations 2.1 where the first is the conservation of mass and the second conservation of momentum:

$$\begin{aligned}\frac{\partial \rho}{\partial t} + \frac{\partial}{\partial x_i}(\rho u_i) &= m, \\ \frac{\partial}{\partial t}(\rho u_i) + \frac{\partial}{\partial x_j}(\rho u_i u_j) &= -\frac{\partial p}{\partial x_i} + \frac{\partial \sigma_{ij}}{\partial x_j} + f_{v,i}.\end{aligned}\tag{2.1}$$

Many simplifications can be made depending on the flow characteristics. One is incompressible flow which is considered valid as long as the velocity is much lower than the speed of sound. The general practice is when the ratio of velocity divided by the speed of sound is less than 0.3. This ratio is also known as the Mach number. Another important non-dimensional number is the Reynolds number (Re) which is inertia over viscosity $Re = \frac{\rho u_i l}{\mu}$ which is used to predict the level of turbulence in a flow. A low number signifies a laminar flow while a high number is equal to turbulence. The number is very dependent on geometry and two different shapes can not be compared [5].

2.1.1 Turbulence

Most of the flow which we encounter in everyday life is turbulent. It can be seen in rivers as well as in cigarette smoke or the flow around a golf ball. The problem with turbulence is that although it has been widely studied no one can actually explain or fully predict the exact behavior of the flow. A few characteristics are typical and could define a turbulent flow [6]:

- **Irregularity:** The flow seems irregular and chaotic but is assumed to be governed by the Navier-Stokes equations creation of turbulent eddies and the destruction in the cascade process together with dissipation.
- **Diffusive:** Increased tendency to spread and blend with nearby flow. Mixing of boundary layer delaying the separation.
- **Three-Dimensional:** Turbulent flow is by nature always three-dimensional although it could be modelled as two-dimensional if the equations are time-averaged.
- **Dissipative:** The largest eddies draw kinetic energy from the flow and the energy is transferred from larger to smaller eddies and finally turned into thermal energy at the smallest eddies. The process is also know as the cascade process.

2.1.2 Computational Fluid Dynamics

To be able to solve complex flow structures the analytic solutions to Equations 2.1 would be too difficult to solve and researchers are left with experimental or numerical methods. As the computational power increases more accurate solutions can be found faster by using CFD which makes it superior to experiments in both cost and time. Experiments are still frequently used to verify the results from CFD.

2.1.2.1 Reynolds Averaged Navier Stokes

Often the need to find average flow characteristics is greater than to find the exact behavior. The RANS equations are based on a time average of Equations 2.1. The velocity and pressure components are decomposed into a mean and a fluctuating value before the equation is time averaged. A term called the Reynolds stress appears which has to be modelled to be solved. Several models have been developed to approximate the stress term and they are all used in different applications.

2.2 Acoustics

Sound is defined as small pressure fluctuations propagating through some transmission medium. These sound waves can travel through many materials, both solids and fluids. The creation of sound by the means of vibrating parts, such as a membrane or a guitar string, has been known for a long time. But it was not until 1952 Lighthill presented his analogy on noise, generated in a fluid flow due to internal shear stresses etc.

Noise is per definition considered as unwanted sound.

2.2.1 Aeroacoustics

Aeroacoustics is the theory of sound generation in a fluid flow. It is derived from the classical wave equation with a source term. Several analogies exist and most of them are based on the Lighthill acoustic analogy.

The classical wave equation is derived from the conservation of mass and momentum given by Equations 2.1. For the equation to be valid the fluid has to be "quiescent" which means that the ambient properties are considered constant in the whole domain. Below is described the method used by Lighthill.

2.2.1.1 Lighthill Acoustic Analogy

The general theory in aeroacoustics was first developed by Lighthill. He used the exact equations of motion of a fluid, without a source, given by Equations 2.2.

$$\begin{aligned}\frac{\partial \rho}{\partial t} + \frac{\partial}{\partial x_i}(\rho u_i) &= 0, \\ \frac{\partial}{\partial t}(\rho u_i) + \frac{\partial}{\partial x_j}(\rho u_i u_j) &= -\frac{\partial p}{\partial x_i} + \frac{\partial \sigma_{ij}}{\partial x_j}.\end{aligned}\tag{2.2}$$

By eliminating (ρu_i) from both equations and subtracting them from each other he obtained Equation 2.3 [7].

$$\frac{\partial^2 \rho}{\partial t^2} - \frac{\partial^2}{\partial x_i \partial x_j}(\rho u_i u_j) = \frac{\partial^2}{\partial x_i \partial x_j}(p \delta_{ij} - \sigma_{ij})\tag{2.3}$$

$$a_0^2 \frac{\partial^2 \rho}{\partial x_i^2} - \frac{\partial^2}{\partial x_i \partial x_j}(a_0^2 \rho \delta_{ij}) = 0\tag{2.4}$$

Equations 2.3 and 2.4 can be added and rearranged into Equation 2.5 where on the left hand side is the wave equation and on the right hand side are the source terms. In a turbulent flow the viscous stresses $\frac{\partial^2}{\partial x_i \partial x_j}(\sigma_{ij})$ can be neglected.

$$\frac{\partial^2 \rho}{\partial t^2} - a_0^2 \frac{\partial^2 \rho}{\partial x_i^2} = \frac{\partial^2}{\partial x_i \partial x_j}(\rho u_i u_j) + \frac{\partial^2}{\partial x_i \partial x_j}(p - a_0^2 \rho) \delta_{ij}.\tag{2.5}$$

Decomposing the flow properties into a mean value and an acoustic fluctuation gives $u_i = u_{0i} + u'_i$, $p_i = p_{0i} + p'_i$ and $\rho_i = \rho_{0i} + \rho'_i$. As it is the perturbations that transfer the sound the mean values are dropped.

$$\frac{\partial^2 \rho'}{\partial t^2} - a_0^2 \frac{\partial^2 \rho'}{\partial x_i \partial x_i} = \frac{\partial^2 T_{ij}}{\partial x_i \partial x_j}\tag{2.6}$$

The term T_{ij} is called the Lighthill stress tensor and represents quadrupole sound sources. The term is defined as:

$$T_{ij} = \rho u_i u_j + (p' - a_0^2 \rho') \delta_{ij}\tag{2.7}$$

In flows at low Mach number where viscous stresses can be neglected, the Lighthill stress term reduces to [8]:

$$T_{ij} \approx \rho_0 u_i u_j \text{ as } p_{ij} = a_0^2 \rho \delta_{ij}\tag{2.8}$$

The Lighthill equation can be written in a form of retarded potentials as below [9]:

$$\rho(\mathbf{x}, t) - \rho_0 = \rho' = \frac{1}{4\pi a_0^2} \frac{\partial^2}{\partial x_i \partial x_j} \int_V \frac{T_{ij}(\mathbf{y}, t - \frac{|\mathbf{x}-\mathbf{y}|}{a_0})}{|\mathbf{x}-\mathbf{y}|} d\mathbf{y}\tag{2.9}$$

2.2.1.2 Acoustic sources

The Lighthill equation does in general only contain the Lighthill stress tensor T_{ij} as the only source. If sources are added to the Navier-Stokes equations as in Equations 2.1 before deriving the Lighthill equation, three sources appear [10]:

$$s_1 = \frac{\partial m}{\partial t}, s_2 = -\frac{\partial f_{V,i}}{\partial x_i}, s_3 = \frac{\partial^2}{\partial x_i \partial x_j} ((p' - a_0^2 \rho') \delta_{ij} + \rho u_i u_j - \sigma_{ij}) \quad (2.10)$$

where the first term s_1 is related to fluctuation mass injection and is called a monopole. The propagation of the monopole is uniform and spreads equally in all directions as can be seen in Figure 2.1 (a). The second term s_2 is called a dipole and is a fluctuating momentum injection which can be compared to a vibrating surface. As can be seen in Figure 2.1 (b) two lobes in a principal direction are shown. The final source s_3 is the same as the Lighthill stress tensor T_{ij} and represents the quadrupole sources. They are the result from turbulent flows and are irregular and are represented by four lobes as can be seen in Figure 2.1 (c) [7].

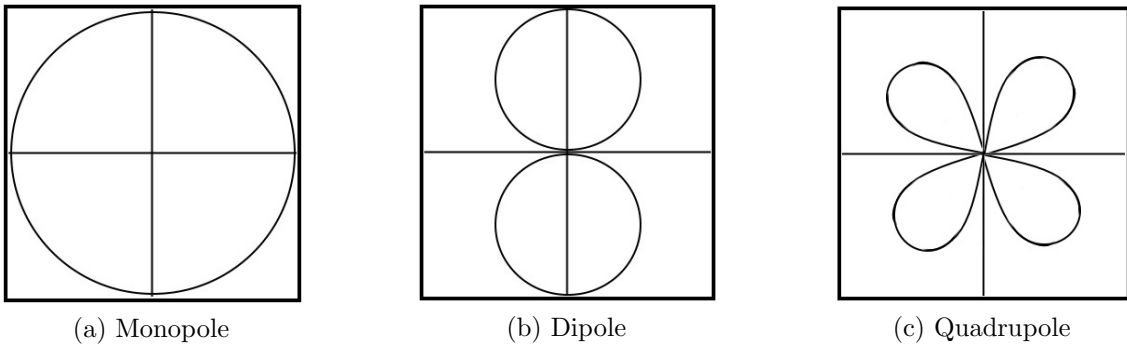


Figure 2.1: The most prominent sources within a fluid flow and the propagation pattern.

2.2.1.3 Broadband Noise Source Models

In Star CCM+ the broadband noise source models can be used to compute the location and power of the different types of noise sources. The name broadband comes from the use of the whole frequency spectra to derive the acoustic energy. Curle, Proudman and Lilley are all sound source models that analyze different types of sources [11].

2.2.1.4 Curle noise source model

When Lighthill formulated his analogy, he did it for a jet engine where no interference from any boundaries was present. Curle rewrote the equation taking rigid surfaces into account and added a source term, taking the dipoles from surfaces into account [9].

The Curle surface integral, Equation 2.11, which is added to the volume integral in Equation 2.9, is used in Star CCM+ [11] to calculate the contribution from the dipole sources in the contact with a surface.

$$\rho'(\mathbf{x}, t) = \frac{1}{4\pi a_0^2} \frac{\partial}{\partial x_i} \int_S \frac{P_i(\mathbf{y}, t - \frac{|\mathbf{x}-\mathbf{y}|}{a_0})}{|\mathbf{x}-\mathbf{y}|} dS(\mathbf{y}) \quad (2.11)$$

where $P_i = -n_j p_{ij}$

The surface acoustic power (SAP) can be used to measure the acoustic power per unit surface area and is calculated from:

$$SAP = \frac{1}{\rho_0 a_0} \left[\int_0^{2\pi} \int_0^\pi \frac{p'^2}{p'^2} |\mathbf{x}-\mathbf{y}|^2 \sin \theta d\theta d\gamma \right] = \int_S I(\mathbf{y}) dS(\mathbf{y}) \quad (2.12)$$

The unit is W/m^2 and if represented in dB, it can be written as:

$$SAP(dB) = 10 \log \left(\frac{SAP}{P_{ref}} \right) \quad (2.13)$$

2.2.1.5 Proudman noise source model

To estimate the level of acoustic noise within a turbulent area Proudman based his work on the methods developed by Lighthill combined with techniques from the statistical theory of isotropic turbulence. He also proposed that the turbulent eddies generating noise are mainly the ones that do not dissipate energy [12]. The noise source model derived, visualizes the acoustic power per unit volume and is written:

$$AP = \alpha \rho_0 \frac{u_{rms}^3}{l} \frac{u_{rms}^5}{a_0^5} \quad (2.14)$$

where α was proposed to be approximately 38.

In Star CCM+ the equation used is slightly altered and uses the turbulence length scale, L , and turbulent timescale, T , as well as a value of α derived by Sakar and Hussaini called α_c which is re-scaled from the original proposed by Proudman and based on Direct numerical simulations (DNS). [11]

The formula for acoustic power used is:

$$AP = \alpha_c \rho_0 \frac{U^3 U^5}{l a_0^5} \quad (2.15)$$

where

$$U = \frac{L}{T}, \alpha_c = 0.629 \quad (2.16)$$

The unit is W/m^3 and represented in dB:

$$AP(dB) = 10 \log\left(\frac{AP}{P_{ref}}\right) \quad (2.17)$$

2.2.1.6 Lilley noise source model

The Lilley Noise source model [11] computes the sources generated by the turbulent shear flow noise around a solid body or in pipe flow. The Lilley equation is defined as:

$$\frac{D}{Dt} \left[\frac{D^2 \Pi}{Dt^2} - \frac{\partial}{\partial x_j} \left(a^2 \frac{\partial \Pi}{\partial x_j} \right) \right] + 2 \left[\frac{\partial u_k}{\partial x_j} \frac{\partial}{\partial x_k} \left(a^2 \frac{\partial \Pi}{\partial x_j} \right) \right] = -2 \left[\frac{\partial u_k}{\partial x_i} \frac{\partial u_j}{\partial x_k} \frac{\partial u_i}{\partial x_j} \right] + \psi \quad (2.18)$$

where:

$$\Pi = \left(\frac{c_v}{c_p} \right) \ln \frac{p}{p_0} \quad (2.19)$$

The entropy fluctuations and fluid viscosity represented by ψ can be omitted in high Reynolds number flows without heat transfer.

The velocity u_i can be decomposed into a time averaged mean part and a fluctuation as:

$$u_i(\mathbf{x}, t) = U_i(\mathbf{x}) + u'_i(\mathbf{x}, t) \quad (2.20)$$

where U_i is the mean velocity and u'_i is the turbulent fluctuation.

$$\begin{aligned} -2 \left[\frac{\partial u_k}{\partial x_i} \frac{\partial u_j}{\partial x_k} \frac{\partial u_i}{\partial x_j} \right] &= -2 \left[\frac{\partial U_k}{\partial x_i} \frac{\partial U_j}{\partial x_k} \frac{\partial U_i}{\partial x_j} \right] - 2 \left[\frac{\partial u'_k}{\partial x_i} \frac{\partial u'_j}{\partial x_k} \frac{\partial u'_i}{\partial x_j} \right] - \\ &6 \left[\frac{\partial U_k}{\partial x_i} \frac{\partial U_j}{\partial x_k} \frac{\partial u'_i}{\partial x_j} \right] - 6 \left[\frac{\partial u'_k}{\partial x_i} \frac{\partial u'_j}{\partial x_k} \frac{\partial U_i}{\partial x_j} \right] \end{aligned} \quad (2.21)$$

The first term on the right hand side represents the changes in the mean flow, the second term, called the self noise term contains only fluctuations and represents the effects from turbulent velocity components and the last two terms together are called the shear noise term and represents the interaction between the mean flow and the turbulent fluctuations.

To generate fluctuations in a time averaged flow a synthetic turbulent field has to be simulated. This is done with the Stochastic Noise and Radiation (SNGR) model [11].

3 Methodology

The work process was divided into four different parts: geometry preparation, case setup, simulation and post processing. The car model was prepared in ANSA v.16.1.0, case set-up, simulation and post-processing were performed in Star CCM+ v.11.06.010.

3.1 Geometry preparation

Before simulations could be performed a CAD-geometry of the car had to be created, prepared and imported into the CFD-program Star CCM+. In addition, the simulation domain surrounding the model had to be created before the cases could be defined.

3.1.1 Car Geometry

The DrivAer car model, developed by the Technical University of Munich [13], used in the simulations was created with the intention to bridge the gap between simplified models such as the Ahmed body and the extremely complex car models used in industry. The geometry is a modular system with several configuration possibilities such as smooth or detailed underbody and different types of rear ends. The geometry deemed suitable for the study can be seen in Figure 3.1. It shows a smooth underbody, notchback rear end, rear-view mirrors and the open rims. The reason the mirrors were kept was to have something which had been studied before as a reference.

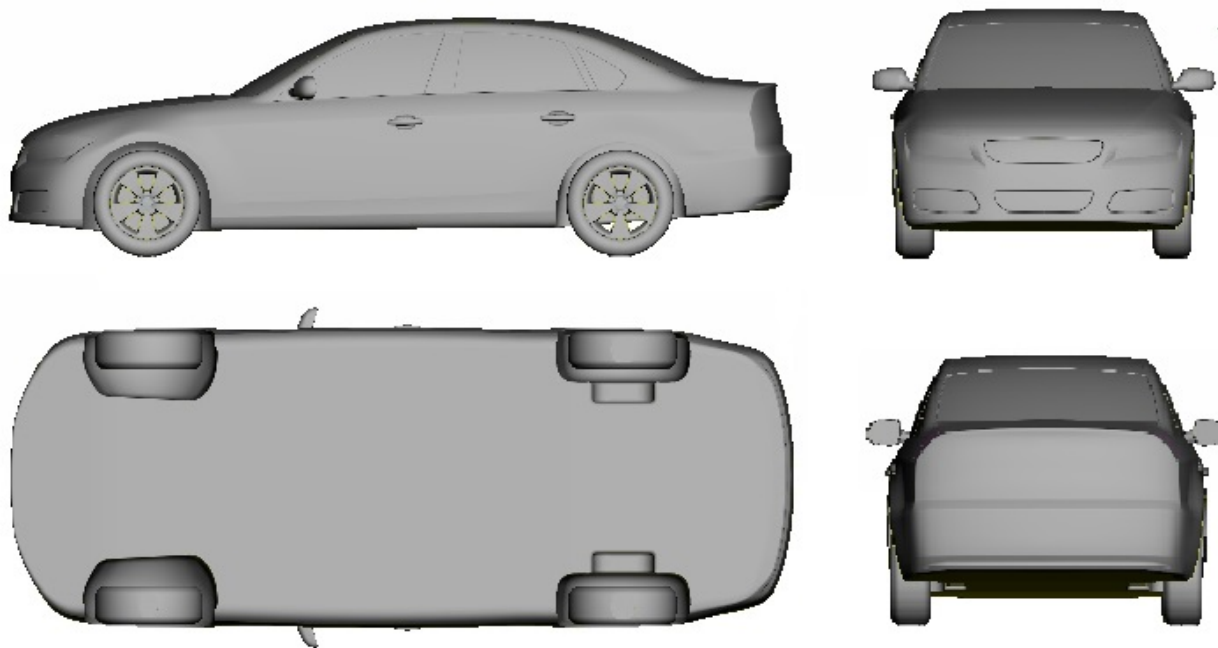


Figure 3.1: The DrivAer model with the smooth underbody, notchback rear end and rear-view mirrors.

Further the geometry consists of several part ids which in simulations can be used to set individual boundary conditions depending on the area of interest. The car model was prepared in ANSA and exported as a Star-CD file. In order to keep the part ids when importing into Star CCM+ the option "Keep material ids" had to be used. The model was then imported as a surface mesh with part mode set to "One part per cell type" in Star CCM+.

In Figure 3.2(a), a closed rim wheel can be seen. The yellow fields seen in the figure are designed with a geometry inside to give the options of having them either as solids or fluids. The volume inside can be used as Moving Reference Frame (MRF)-zones in simulations to fake a rotation of the wheels and they can also be used as a solid boundary depending on preferences. As a reference, Figure 3.2(b) shows the rims when the inner geometry is displayed.

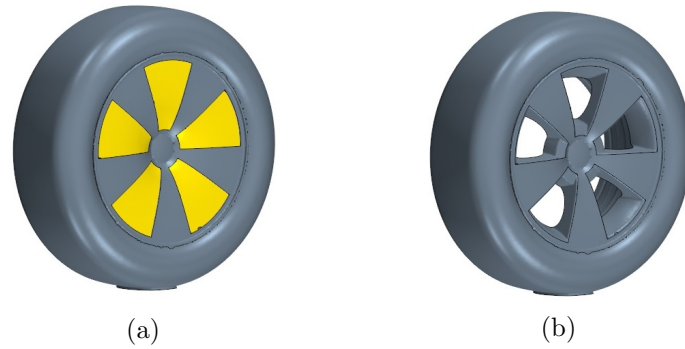


Figure 3.2: The two settings of the rims used (a) Closed rims with the MRF-zones marked in yellow (b) Open rims.

3.1.2 Computational domain

The computational domain is the area surrounding the car model and can be seen in Figure 3.3. The dimensions of the domain are 50x10x10 m and the car is placed approximately 15 m from the inlet [14]. In order to decrease the number of cells used, half of the car was used. In addition, three volumes called refinement boxes were created to prepare for the mesh generation. The three refinement boxes, covering the ground, around the car and around the wheel area, were placed as can be seen in Figures 3.3 and 3.4.

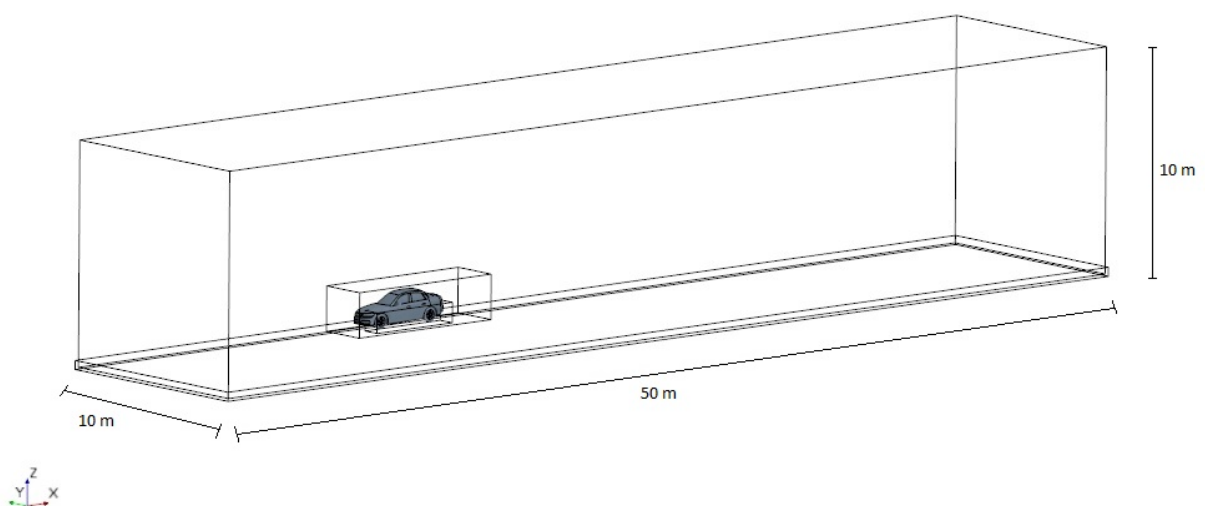


Figure 3.3: Three dimensional overview of the computational domain together with refinement boxes. The front of the car model is located approximately 0.75 m downstream of origo. The inlet is set at -15 m and the outlet at 35 m in the x-direction. $y=0$ is at the symmetry line cutting through the car and $z=0$ is at the ground.

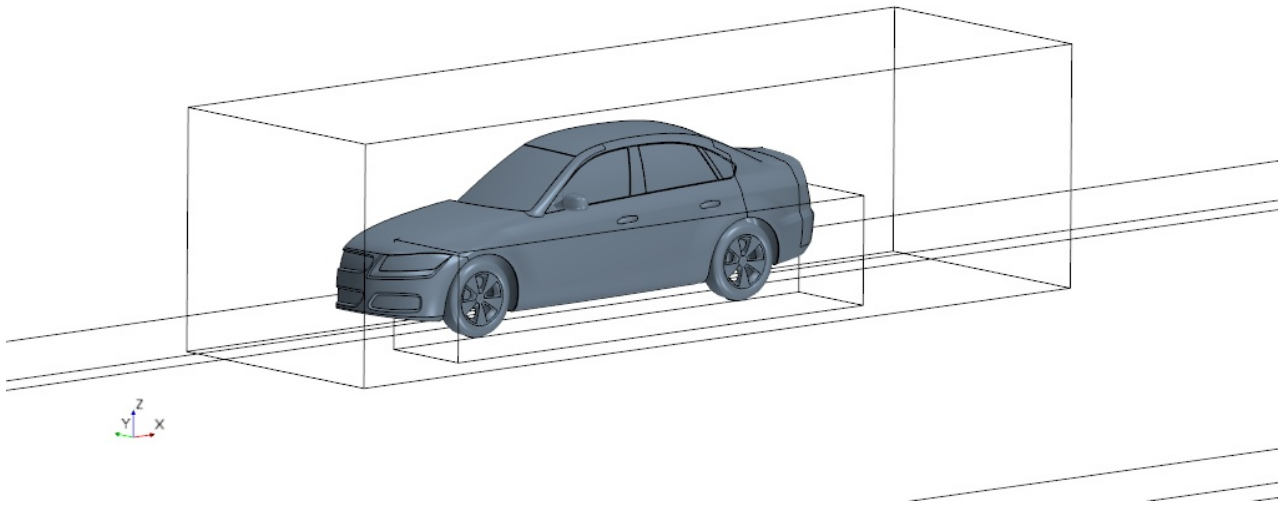


Figure 3.4: The refinement boxes used.

3.2 Case setup

Four cases had to be created to simulate the different setups of non-rotating/rotating wheels combined with closed and open rims. The goal was to make the four cases as similar as possible to improve the comparability between the cases. The cases are listed in Table 3.1.

Table 3.1: Case settings

Case	Open/Closed rims	Stationary/Rotating wheels
Case 1	Closed	Stationary
Case 2	Closed	Rotating
Case 3	Open	Stationary
Case 4	Open	Rotating

3.2.1 Mesh generation

To make the four cases as equal as possible the same geometry was used for all cases. A desire was to set up all cases with MRF-zones and just change the boundary conditions to solid on the contact surface on the closed rims cases. That rendered errors in the Lilley solver and the MRF-zones had to be deleted in the closed rims cases, for it to work. This did not in any way alter the simulation results. The meshing procedure was to first use a surface wrapper to enclose the car geometries and make sure there were no gaps or other impurities in the model. Due to the gap between the car body and the wheels, three wrappers had to be used. The settings that were changed from standard are given in Table 3.2. The same settings were used on both wheels and the body.

Table 3.2: Surface Wrapper Settings

Property	Option	Value
Base Size	N/A	10 mm
Surface Curvature	Basic Curvature	60 pts
Volume of Interest	External	N/A

For the solver program to understand that there is a solid body inside the domain a subtract had to be done before volume mesh was applied. Then an automated mesh was created inside the subtracted domain. The trimmed cell mesh was used in the volume, for its robustness and independence from surface quality. In Figure 3.5, the domain is seen from the side showing the refinement close to the ground and around the car. The gradual increment of the cell size can be seen as well as wake refinement. In Figure 3.6, a view closer to the car shows the refinement along the side of the car set to resolve the sound generated around the wheels. The wake refinement is present also here.

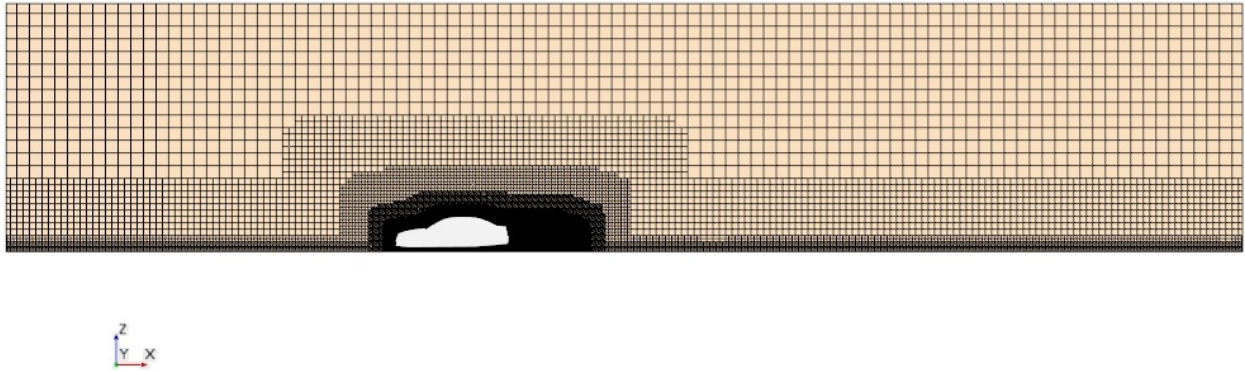


Figure 3.5: Side view of the full domain containing the volume mesh with the refined mesh at the ground and around the car.

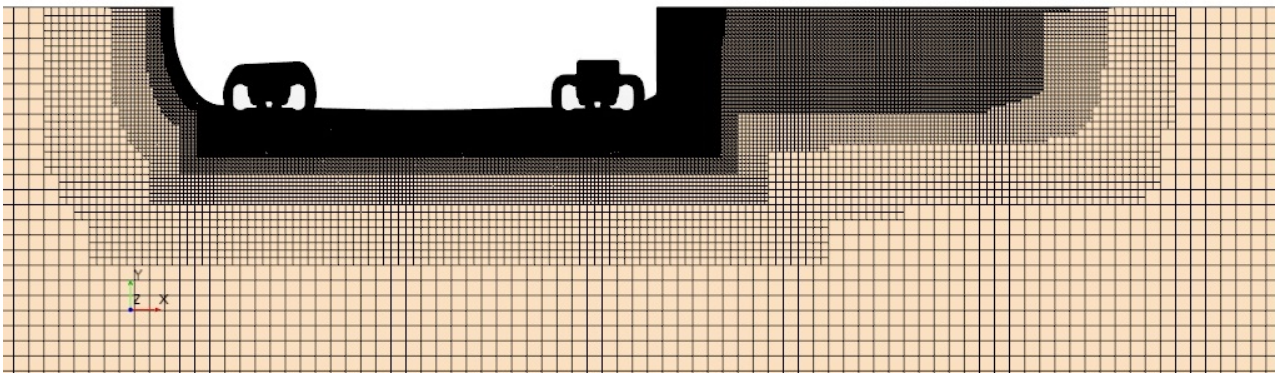


Figure 3.6: Close up on the car seen from the top and through the wheels showing refinements in the wake and around the wheels.

At the surface, the prism layer mesher is used to accurately resolve the near wall flow. The prism layer consists of 12 layers spread over 8 mm and the first layer height is 0.0125 mm giving a y^+ of approximately 1. The prism layers can be seen in Figure 3.7 together with the finest mesh around the wheels which is 4 mm in size. A perfect mesh with regard to cell size, to fully resolve every aspect around the car, is not justified regarding the computational time.

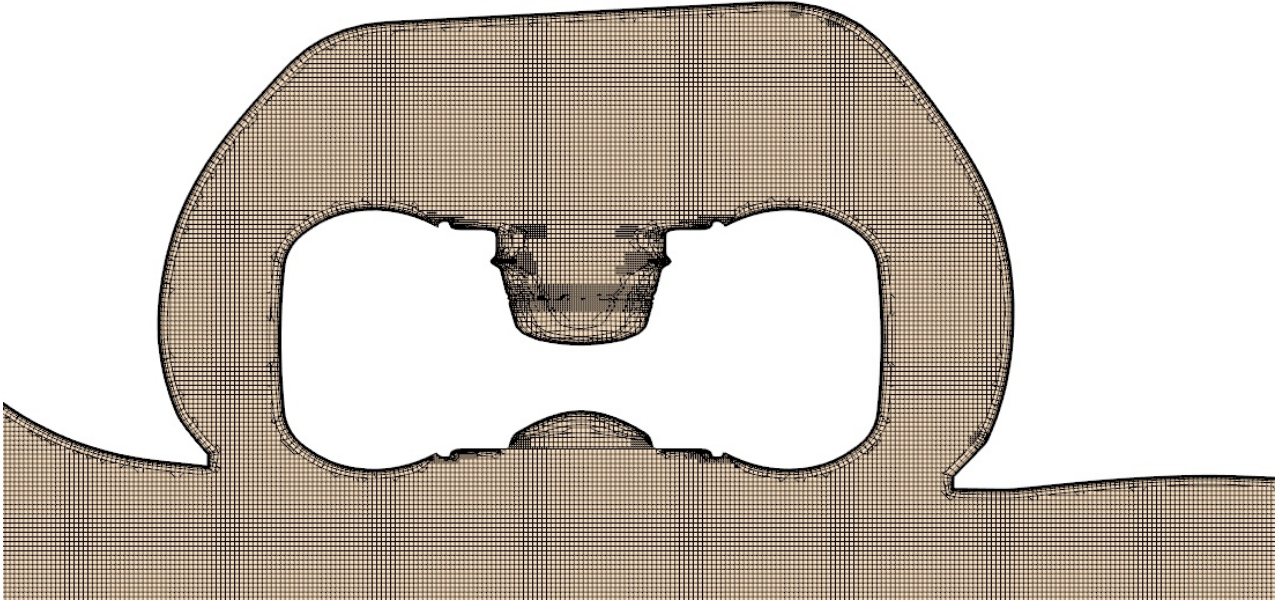


Figure 3.7: The mesh around the front wheel seen from the top showing the finest cell size.

3.2.2 Physics setup

After the mesh was generated, solvers and boundary conditions had to be set up. Due to the nature of the acoustic solvers, all cases had to be simulated as steady state RANS with a 2-equation turbulence model and the model chosen was the realizable $k-\epsilon$, as it is the most commonly used [15]. Further constant density and segregated flow parameters were chosen. The acoustic models need only one iteration to be solved, and can advantageously wait until convergence is met. Proudman and Curle can be solved together while Lilley needs to be solved separately with its own solver. Therefore, a separate file had to be created for the Lilley solution to allow for simultaneous post-processing.

All simulations used the free stream velocity of 36 m/s \approx 130 km/h. For the rotating cases a coordinate system was placed in each wheel center and a reference frame associated to it. The rotation of the wheels was set to 18 rps. The moving ground to the same velocity as the free flow.

3.3 Simulation

To facilitate the simulations, time was given at the Chalmers Centre for Computational Science and Engineering (C3SE), a computational cluster provided by the Swedish National Infrastructure for Computing (SNIC). Each simulation used five nodes at the cluster and each node consisted of 20 cores. To measure convergence a combination of residuals, the drag coefficient C_d and a surface area averaged value of Curle Acoustic Power was used. Due to a relatively coarse mesh at areas outside of interest, C_d was allowed to fluctuate within four counts for about 500 iterations to be considered converged.

Table 3.3 shows the number of cells used in the domain, number of iterations needed to achieve convergence of C_d as well as the time needed multiplied by the number of cores, based on 500 iterations per hour, for the simulations to converge.

Table 3.3:

Case	Mesh size	Iterations	CPU time
Case 1	52.0M	14500	2900
Case 2	52.0M	6000	1200
Case 3	52.4M	15300	3100
Case 4	49.5M	8000	1600

3.4 Post-processing

When a simulation had reached sufficient convergence the results were extracted with a variety of tools.

- Plane section: A plane section is a slice cut through the domain where results can be presented. It is very good when a visualization of gradients or a full spectra of e.g. velocities is of value.
- Isosurfaces: When a specific value is evaluated within the domain an isosurface is useful to visualize areas where that value can be found.
- Streamline: This is especially useful when one want to see how specific particles move through the flow.

4 Results and Discussion

The results from the simulations are presented in this chapter, divided into flow characteristics and acoustic sound sources.

4.1 Flow characteristics

To understand the mechanics of aeroacoustics, some characteristics of the flow are necessary to investigate. Here the characteristics of pressure and velocity magnitude will be shown.

4.1.1 Pressure

The Bernoulli equation shows that pressure is inversely related to velocity, and simplified it means that high velocity gives low pressure and vice versa. In Figure 4.1 it can be seen that a high pressure area is located where the flow impacts the tire and a low pressure area where the flow later accelerates around the tire. In Cases 2 and 4 where the wheels are rotating the high-pressure areas are identical to the non-rotating cases. The low-pressure areas on the other hand show that the pressure is lower when the wheels are rotating which can be explained by the added velocity from the rotation of the wheel.

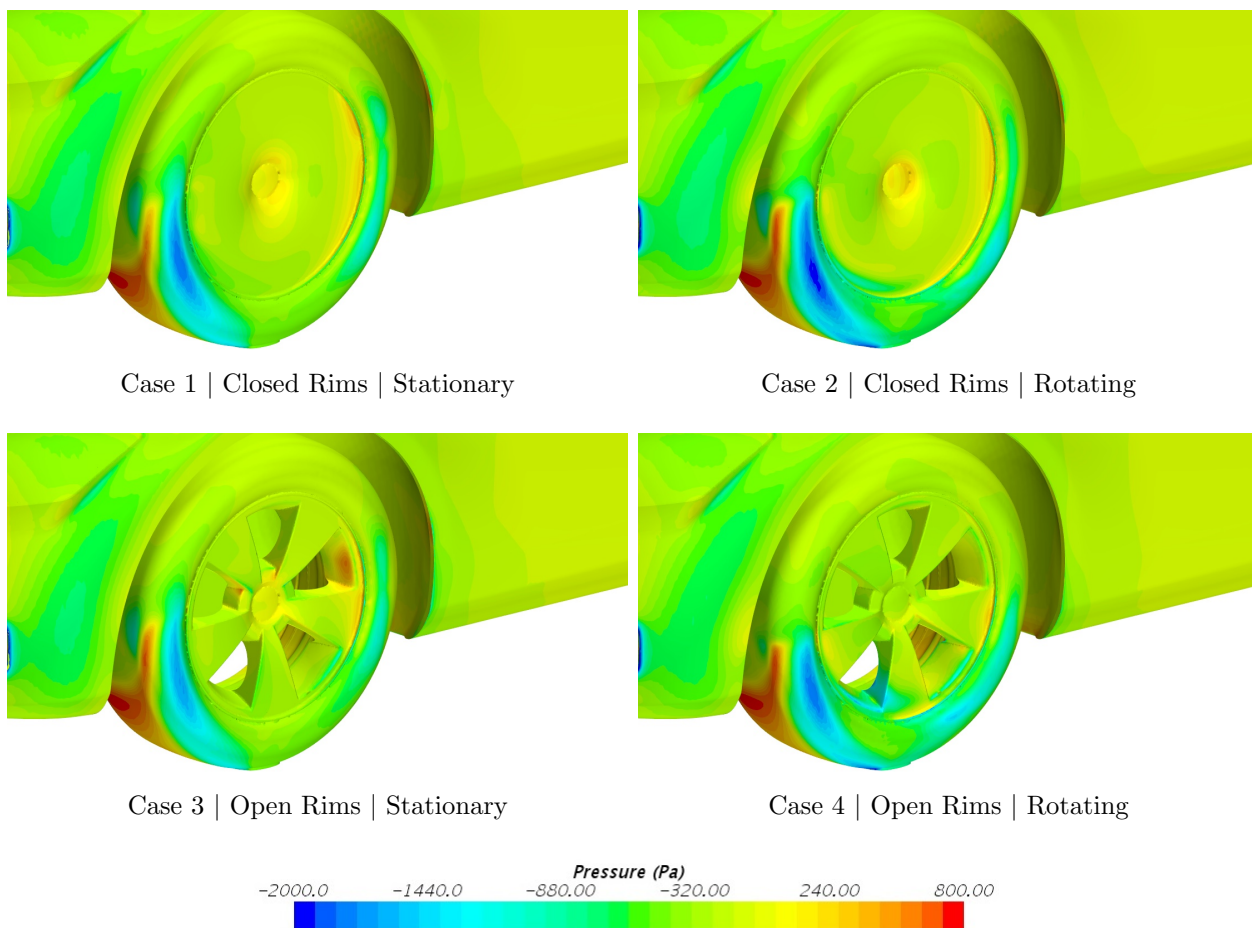


Figure 4.1: A comparison of pressure profiles on the front wheels in the four cases.

4.1.2 Velocity

Three cut-planes are used at different heights from the ground to visualize the flow past different parts of the wheels. They are presented from upper to lower and visualized as both velocity magnitude and turbulent kinetic energy (TKE). In Figure 4.2 the locations of the three planes are shown from the front. In the upper location, the tire can be seen hidden behind the front spoiler and in the middle, it is partly exposed. In the lower plane the tire is completely exposed to the flow. The effect of the different levels of exposure to the flow will be discussed here.

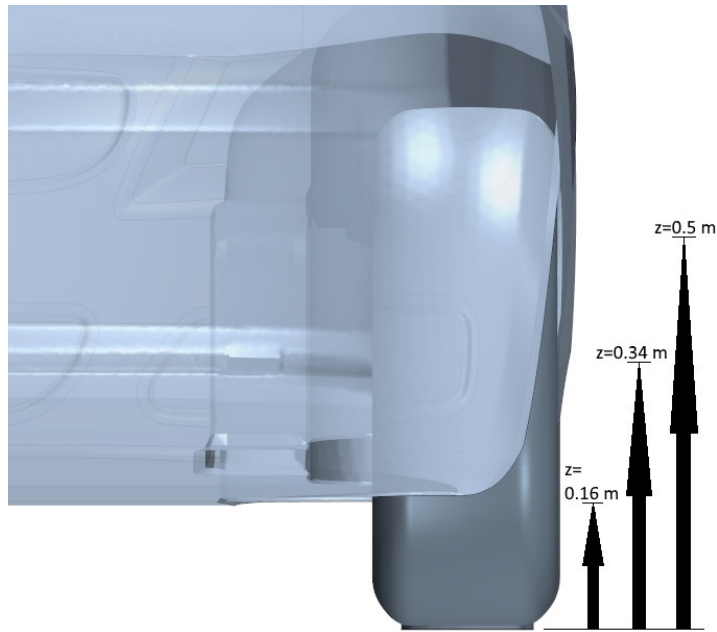


Figure 4.2: Locations of the cut-planes studied.

4.1.2.1 Velocity magnitude at $z = 0.5$ m

In a steady state flow, which has been studied here, the velocity profile alone, cannot give the full picture of what is happening in the flow. Together with the turbulent energy though a better understanding can be given. By studying the separation of boundary layers and what occurs inside is necessary to predict noise.

By looking at Figure 4.3, at the upper part of the wheel, there are many similarities seen between the cases. All of them have the same point of separation and the shape of the boundary layer is very similar. In Cases 2 and 4 the rotation seems to delay the expansion of the boundary layer slightly compared to Cases 1 and 3. In Cases 2, 3 and 4 the velocity profiles show a stagnated area, but together with Figure 4.4 it is clear that what seems stagnant is actually highly turbulent flow with a mean value close to zero. It can also be seen that both rotation and shape of the rims contribute to the turbulence. By comparing Case 2 with Case 3 in Figure 4.4 it can be assumed that the rotation gives a greater contribution to the TKE than the geometry. It can also be seen in Case 4 that the combination of rotation and open rims gives a very high turbulent energy.

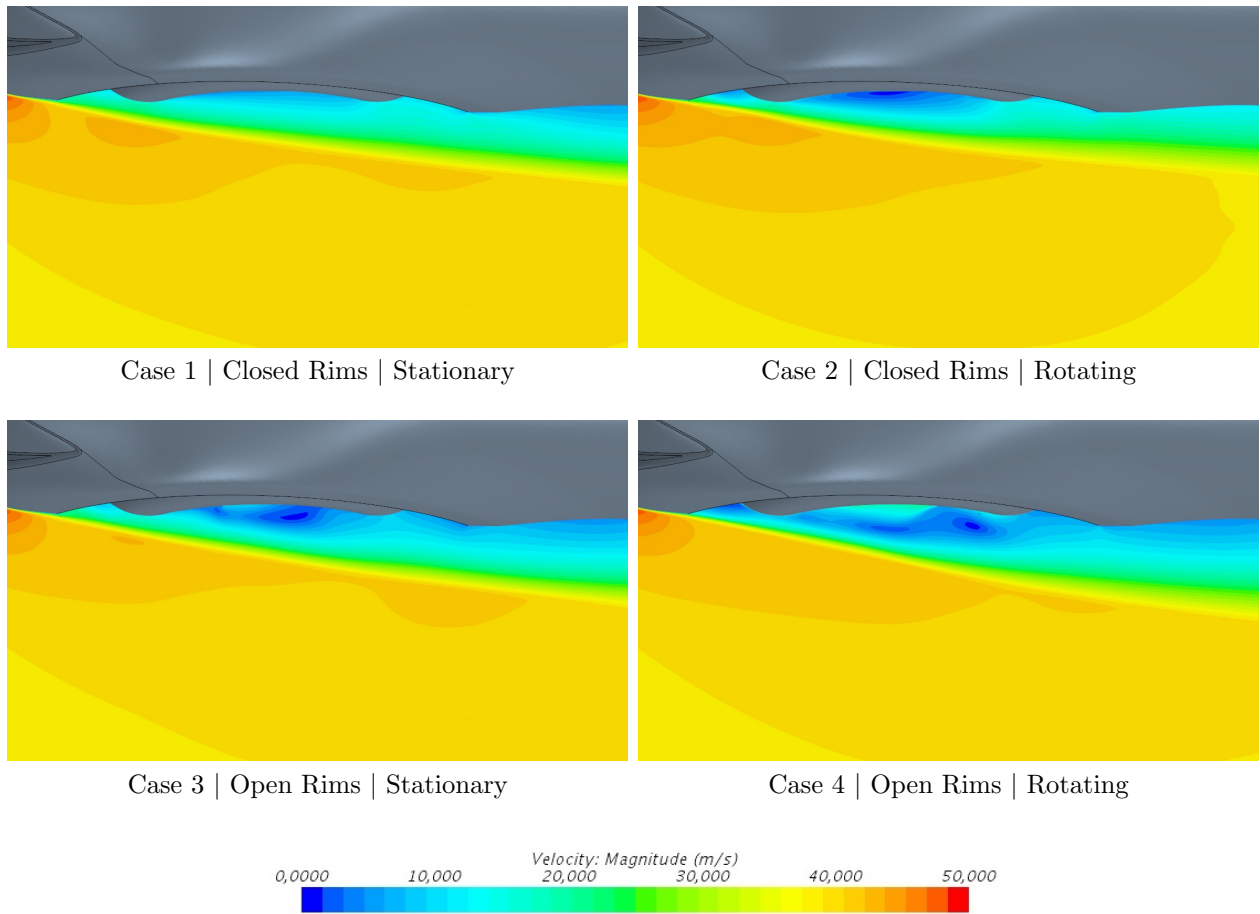
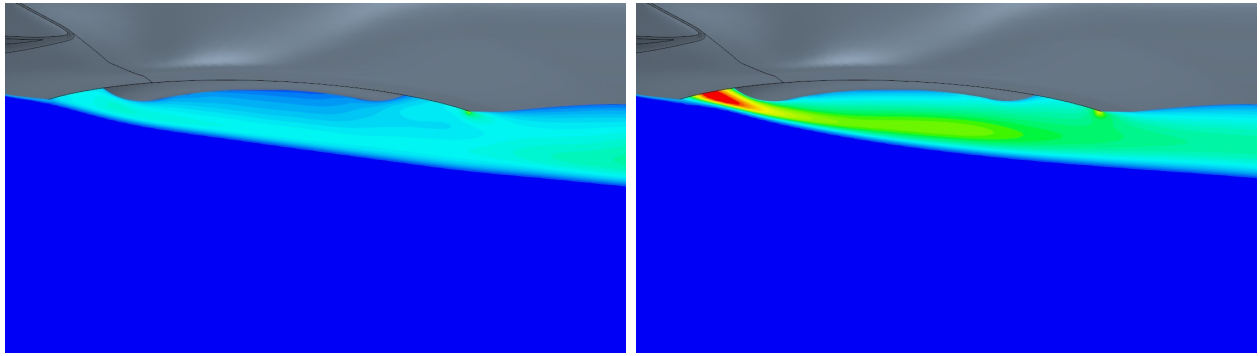
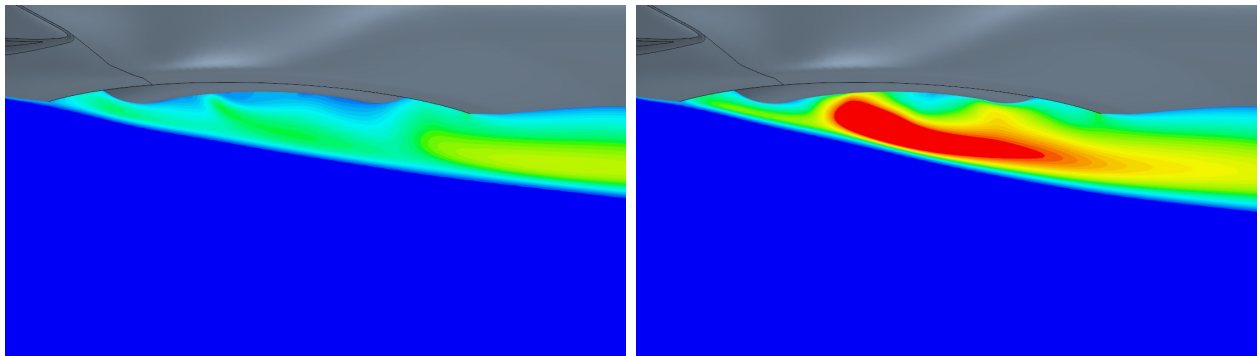


Figure 4.3: Velocity magnitude profiles at $z=0.5$ m.



Case 1 | Closed Rims | Stationary

Case 2 | Closed Rims | Rotating



Case 3 | Open Rims | Stationary

Case 4 | Open Rims | Rotating

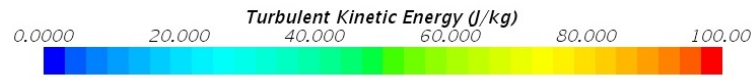


Figure 4.4: Turbulent Kinetic Energy profiles at $z=0.5$ m.

4.1.2.2 Velocity magnitude at $z = 0.34$ m

At the center of the wheel as in Figure 4.5, some differences are much more apparent. In Cases 1, 2 and 3 the tire interferes with the boundary layer expansion and the flow accelerates around it back in toward the body. Contrary to the upper part of the wheels, the rotation appears to expand the boundary layer faster. This can be explained by the fact that the rotation forces the flow down closer to the center which creates a lower pressure at the top and higher pressure at the center. This leads to a lower pressure in Cases 2 and 4, of Figure 4.3, sucking the flow inward, while a higher pressure is present in Figure 4.5 pushing it outward. In Figure 4.6, Case 2 shows that the turbulent energy is not sufficient to create enough pressure to separate the flow from the contact point and a weaker recirculation bubble can be seen. In Case 4 the boundary layer expands fast enough to not interfere with the tire and a highly turbulent area can in Figure 4.6 be seen inside the boundary layer.

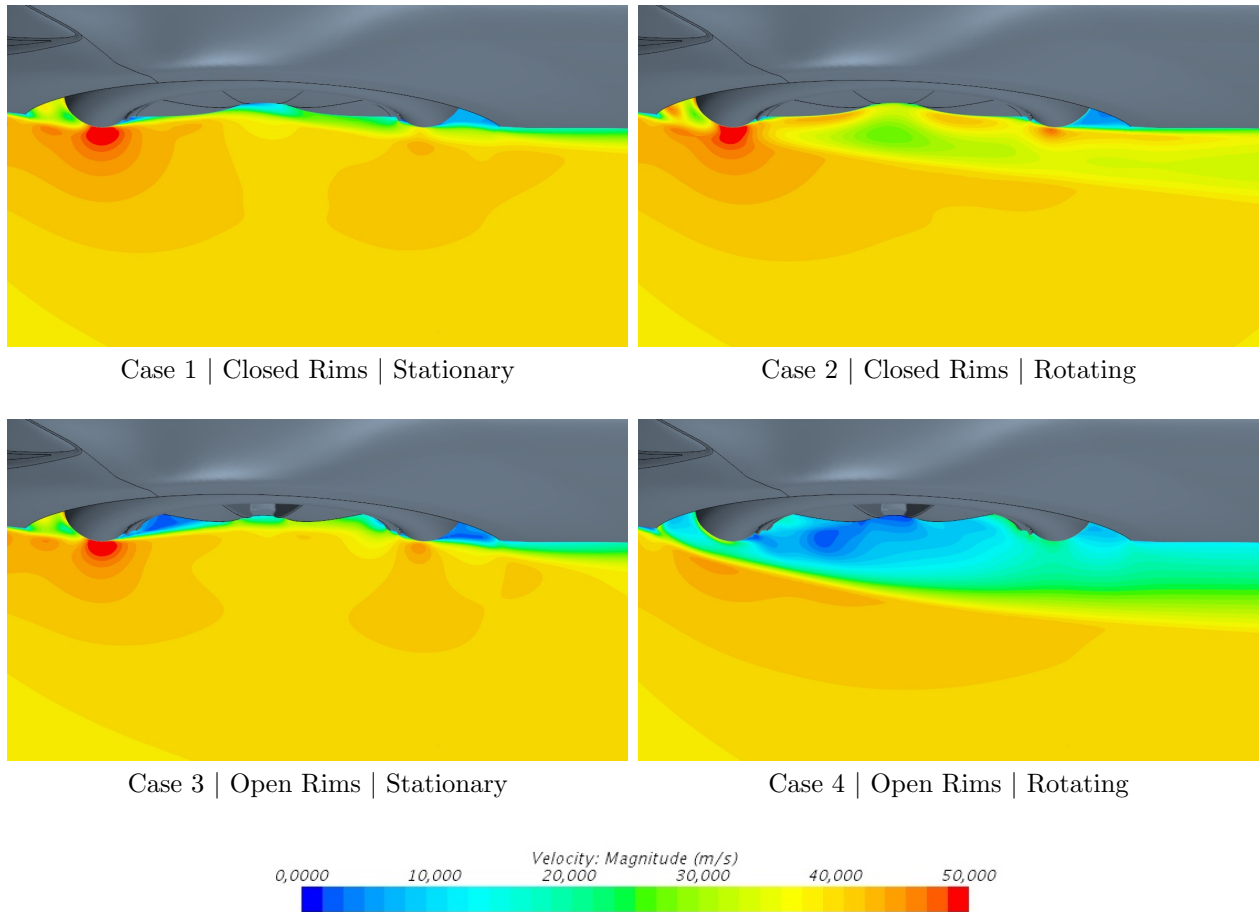


Figure 4.5: Velocity magnitude profiles at $z=0.34$ m.

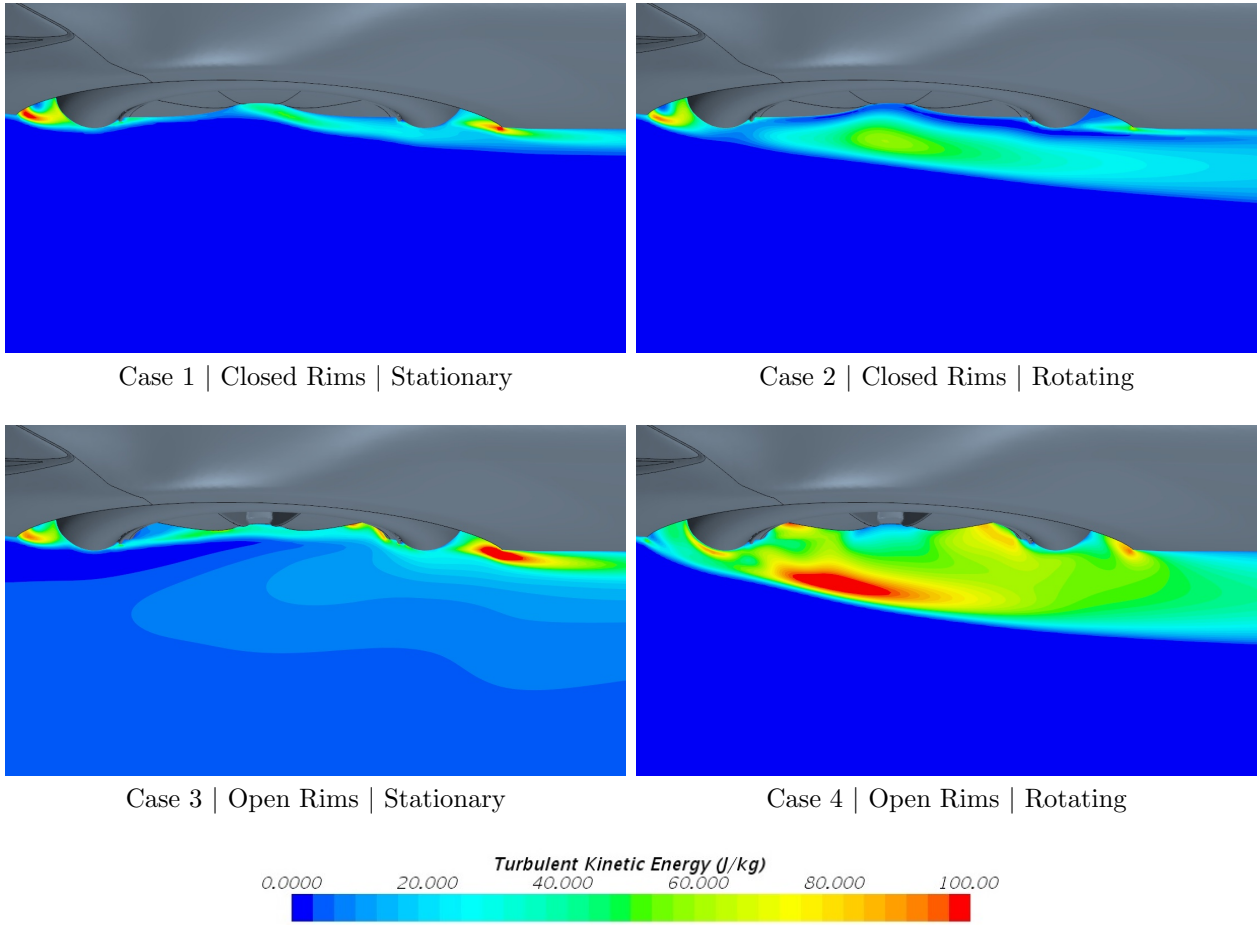


Figure 4.6: Turbulent Kinetic Energy profiles at $z=0.34$ m.

4.1.2.3 Velocity magnitude at $z = 0.16$ m

In the lower part of the wheel seen in Figure 4.7 the cut is made under the body of the car and the flow impacts the wheel directly. This leads to the lack of a separated boundary layer in the front of the wheel. The flow accelerates around the tire and stays close to the wheel all the way past. It is not until after the wheel a more or less visible boundary layer appears. It is apparent when looking at TKE in Figure 4.8 that the ground in the stationary Cases 1 and 3 has an influence on the spreading of the turbulence. In all cases, the TKE is concentrated to the area behind the wheel, although in Cases 3 and 4 a lot of turbulence is seen between the spokes of the rims.

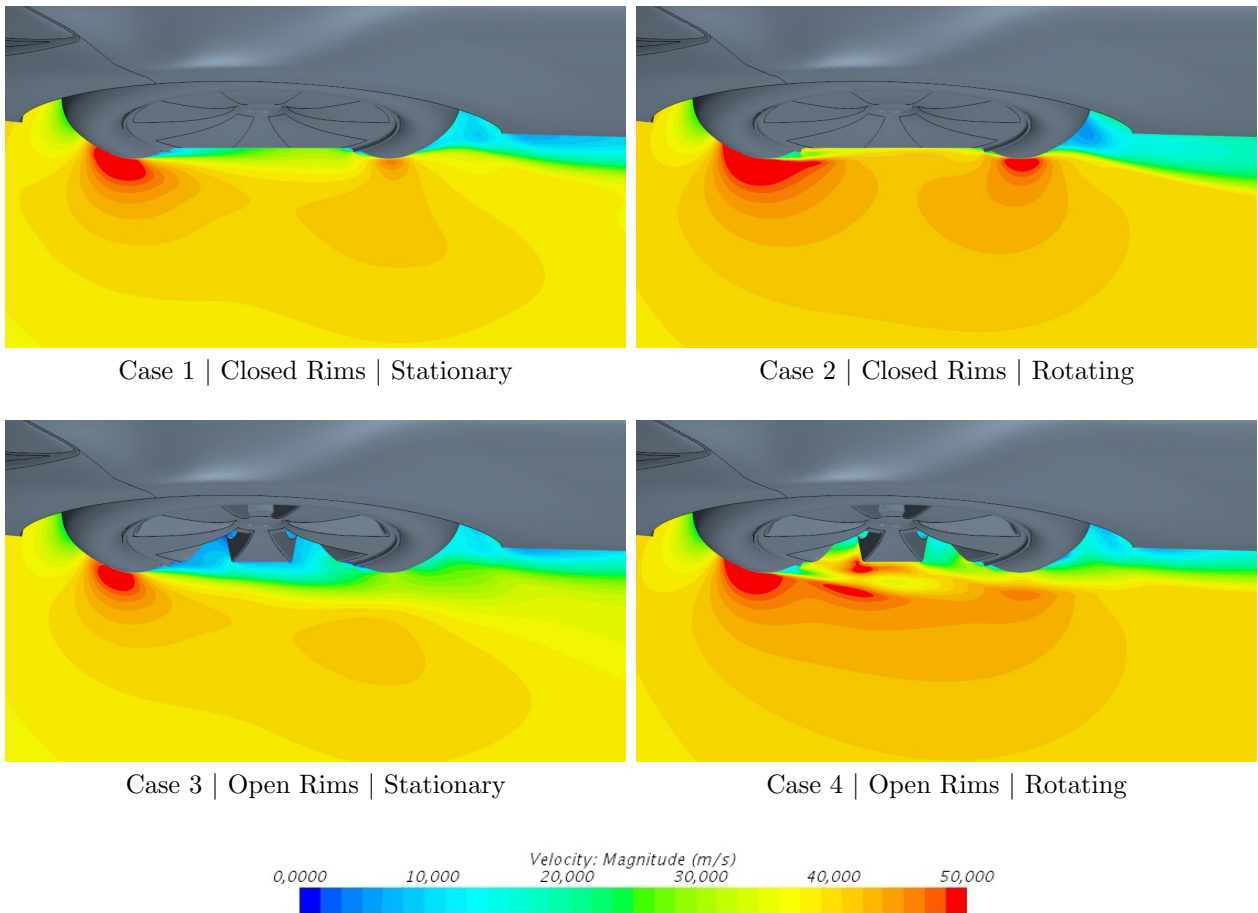


Figure 4.7: Velocity magnitude profiles at $z=0.16$ m.

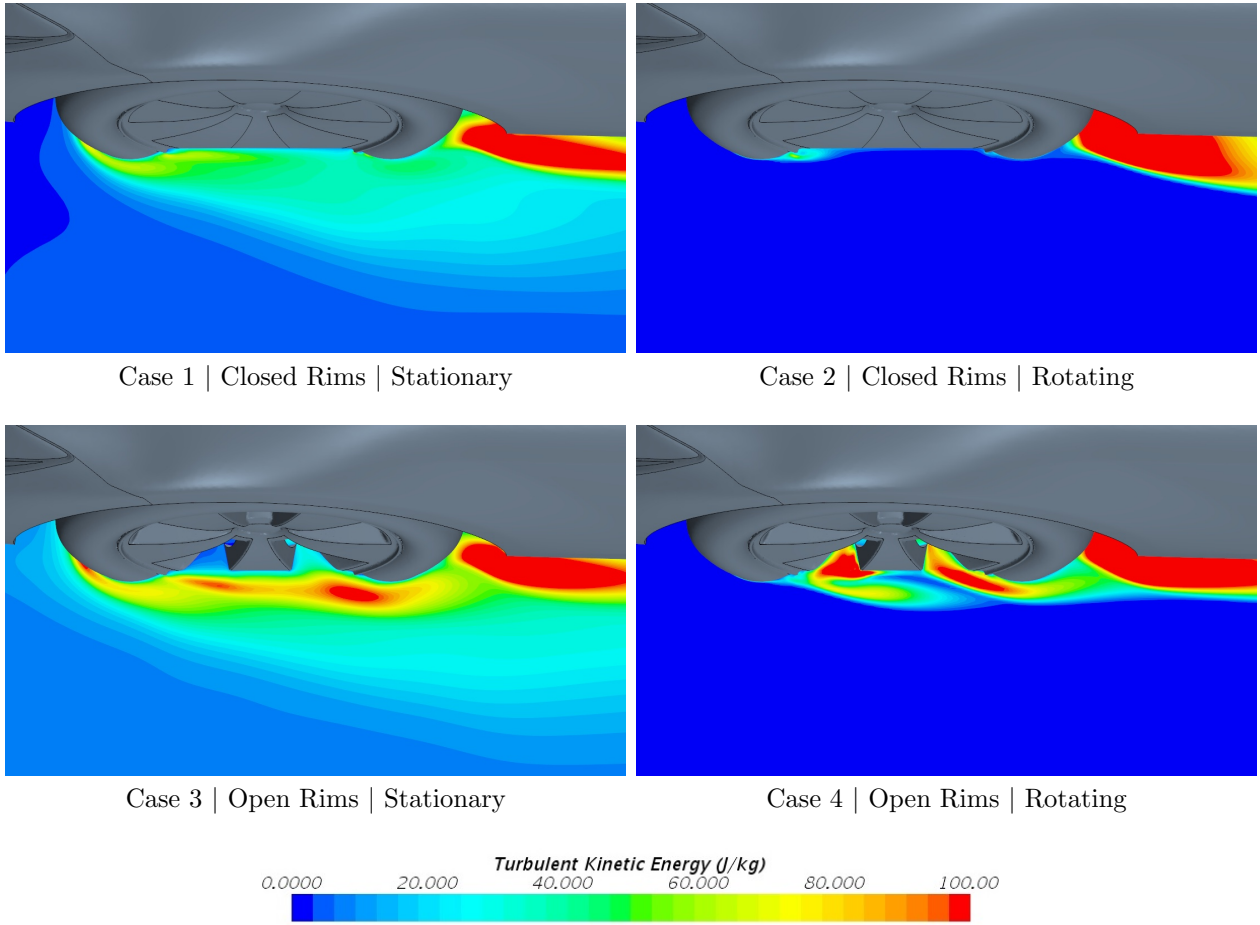


Figure 4.8: Turbulent Kinetic Energy profiles at $z=0.16$ m.

4.2 Acoustic sound sources

In aeroacoustics, there are several methods to measure sound sources. The models used here, are the Curle surface acoustic power (SAP), Proudman acoustic power (PAP) and Lilley turbulent shear flow noise.

4.2.1 Curle Noise Source Model

One way to measure the noise within a fluid is to analyze the turbulent boundary layer when pressure fluctuations are influenced by a solid boundary. The Curle model visualizes the dipoles created on the surface of the car. As can be seen in Figure 4.9, Cases 1 and 3 show a moderate level of noise on the front wheels where the flow impacts after rounding the front spoiler. The magnitude is similar to what is seen on the rear-view mirror and A-pillar. Hardly anything can be seen on the rear wheels. When the wheels are set to rotate, as in Cases 2 and 4, the magnitude of the SAP increases drastically at the points of impact on the front wheels. The increase is significant on the rear wheels as well, although still much lower than on the front wheels. The much lower power seen on the rear wheels can mainly be explained by lower velocities around the wheel as well as the lower turbulent energy.

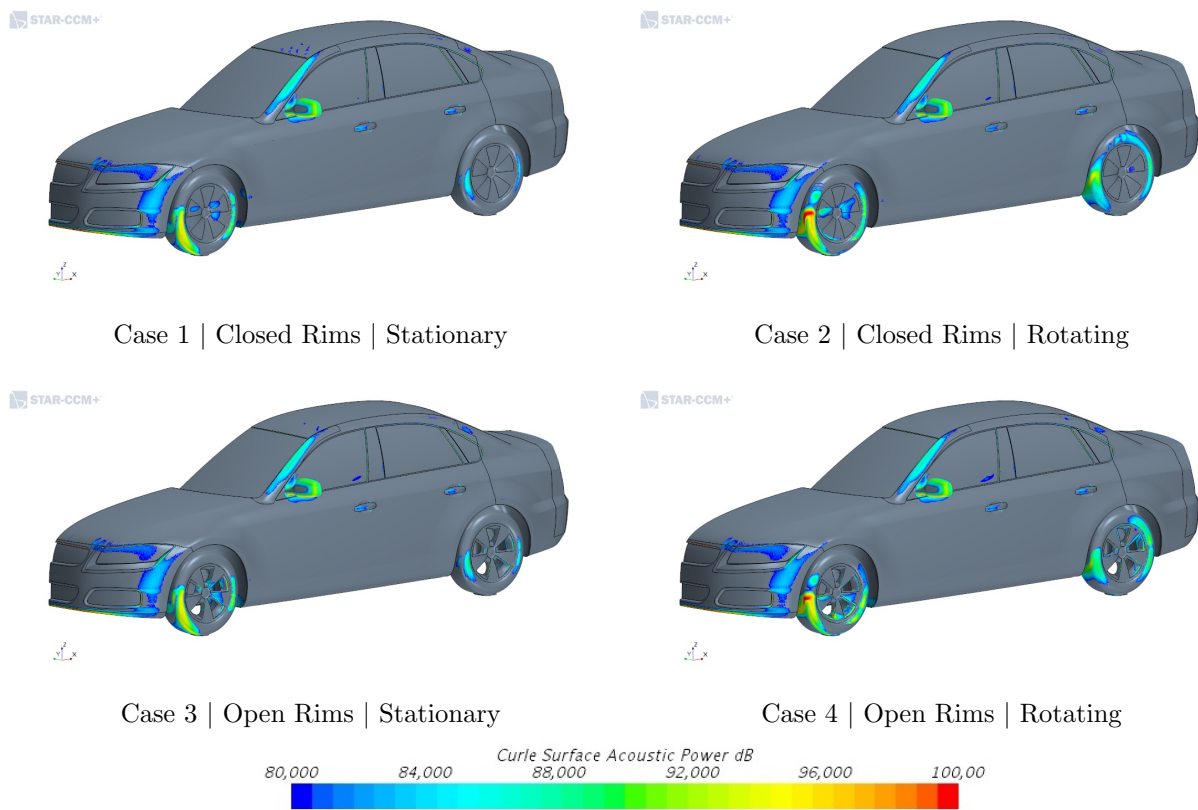


Figure 4.9: Curle Surface Acoustic Power visualized in the range of 80 to 100 dB.

As can be seen in Figure 4.10, there is no significant difference between Cases 1 and 3 in neither noise nor flow characteristics. Regarding Cases 2 and 4, it can be noted a slightly larger area of high intensity in Case 2. Even though there is a small difference seen between Cases 2 and 4, it can be concluded that the design of the rims has much less impact on the dipole sources than the rotation. By studying the structure of the flow in Figure 4.10, when it enters the wheelhouse, it is clear that the high noise areas correlate with the impact of the flow rounding the car body. It can also be seen that the rotation of the wheel prevents the flow to spread up over the wheel and thus forcing more of the flow to impact the wheel in a smaller area causing more noise at that specific location.

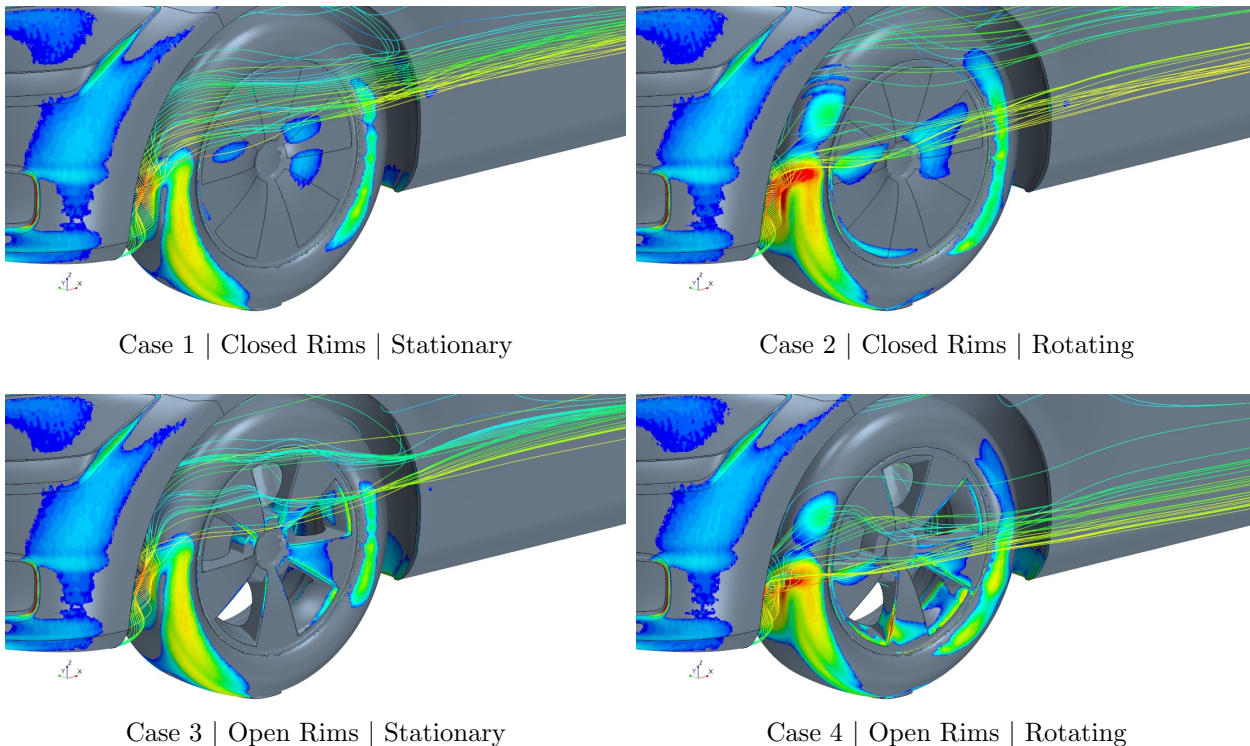


Figure 4.10: A visualization of Velocity streamlines over Curle Surface Acoustic Power sound sources.

When looking at the maximum values of the curle sources, it can be seen in Table 4.1, that the influence from the change in geometry of the rims, is negligible compared to the contribution from rotation.

Table 4.1: Maximum Curle Surface Power.

Case	Value (dB)
Case 1	96
Case 2	102
Case 3	96
Case 4	102

4.2.2 Proudman Noise Source Model

The Proudman acoustic model visualizes the acoustic power per unit volume which is generated by the quadrupole sound sources of the flow. Some comparisons are made at the power levels of 70, 80 and 90 dB. In Figure 4.11 below, the isosurfaces represent the area of noise at 70 dB. What can be seen is that in the stationary cases the main part of the noise is located near the ground which could be partially explained by the stationary ground. In the rotating cases, much more of the noise comes from the upper part of the wheel. At this magnitude, it is hard to see if there is more or less noise in any of the cases. But, as the quadrupole sources contain the Reynolds-stresses it is straight forward to assume that the intensity increases when the geometry gets more complex as well as with rotation.

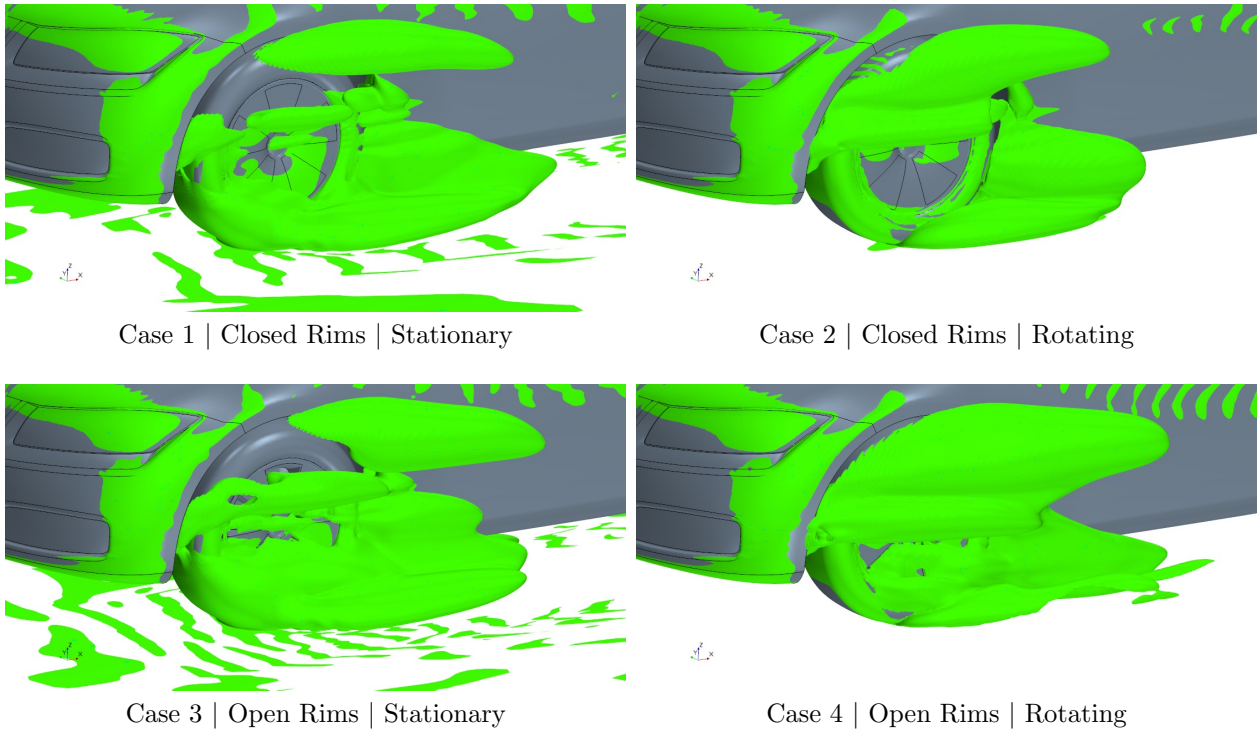


Figure 4.11: Isosurfaces showing Proudman Acoustic Power sound sources at 70 dB.

At 80 dB the influence of the rims is much more apparent and the difference between open and closed rims is obvious. When looking at Cases 1 and 2 in Figure 4.12, it can be seen that the rotation hardly changes the appearance at all. It is reasonable, as there is no structure that could rotate the air as there is with open rims. In Case 4 the air between the spokes rotates together with the wheel and the sound sources get more evenly distributed around the wheel. A major source is in all cases located behind the wheel although the open rims produce a great part of the noise between the spokes. As was seen in Figure 4.11, the fourth case displays a large area of noise production, in the upper part of the wheels, that cannot be seen in the other cases.

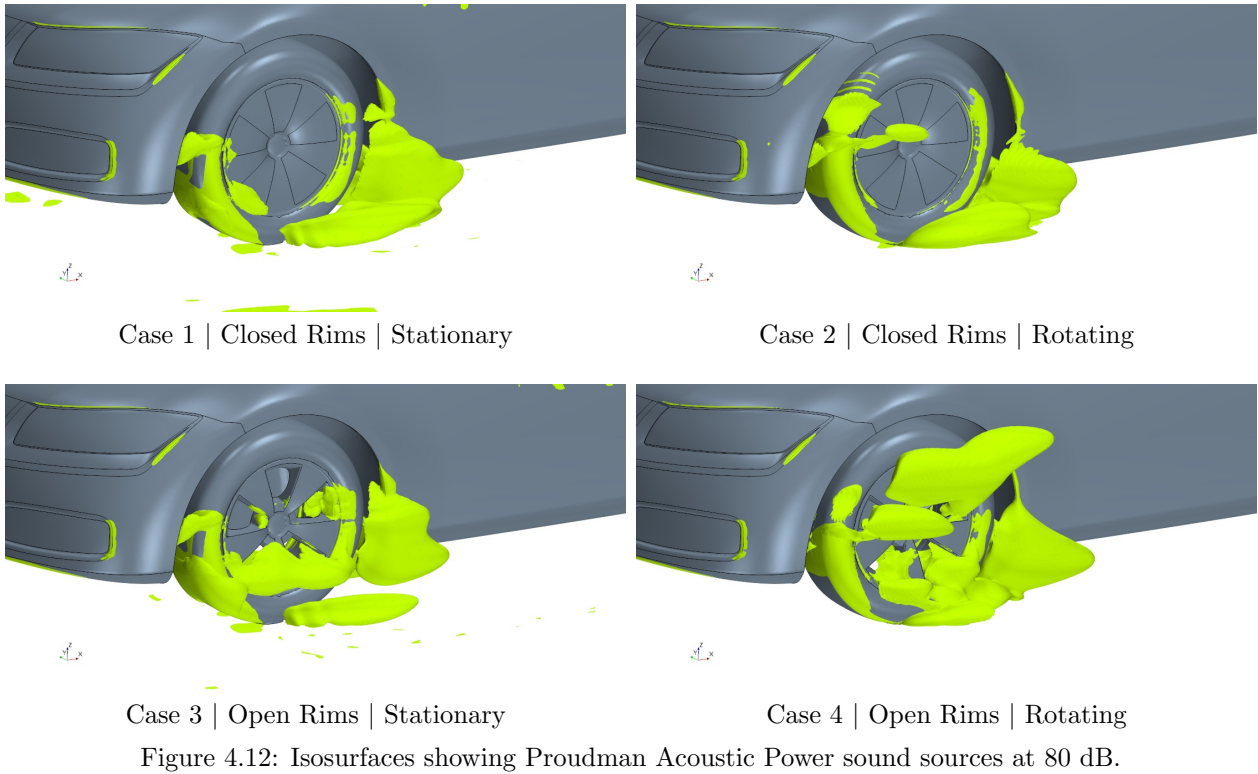


Figure 4.12: Isosurfaces showing Proudman Acoustic Power sound sources at 80 dB.

When the noise level evaluated is increased to 90 dB the location of the most distinct source is the same for all cases. In the stationary cases in Figure 4.13 the shapes of the sources are both of a pear with a slightly larger volume on the open rim case. When the wheels are rotated the volume increases drastically and what is not expected is that in Case 2 the source area is shifted slightly closer to the wheel and shaped differently than the others. Also, here a difference can be seen between open and closed rims but not as significant as between the stationary and rotating cases. At the front of the wheels a source much similar, in shape, to the Curle surface sources can be seen in all cases. There are also many smaller sources in between the spokes of the rims. Specifically in the case when the wheels are rotating.

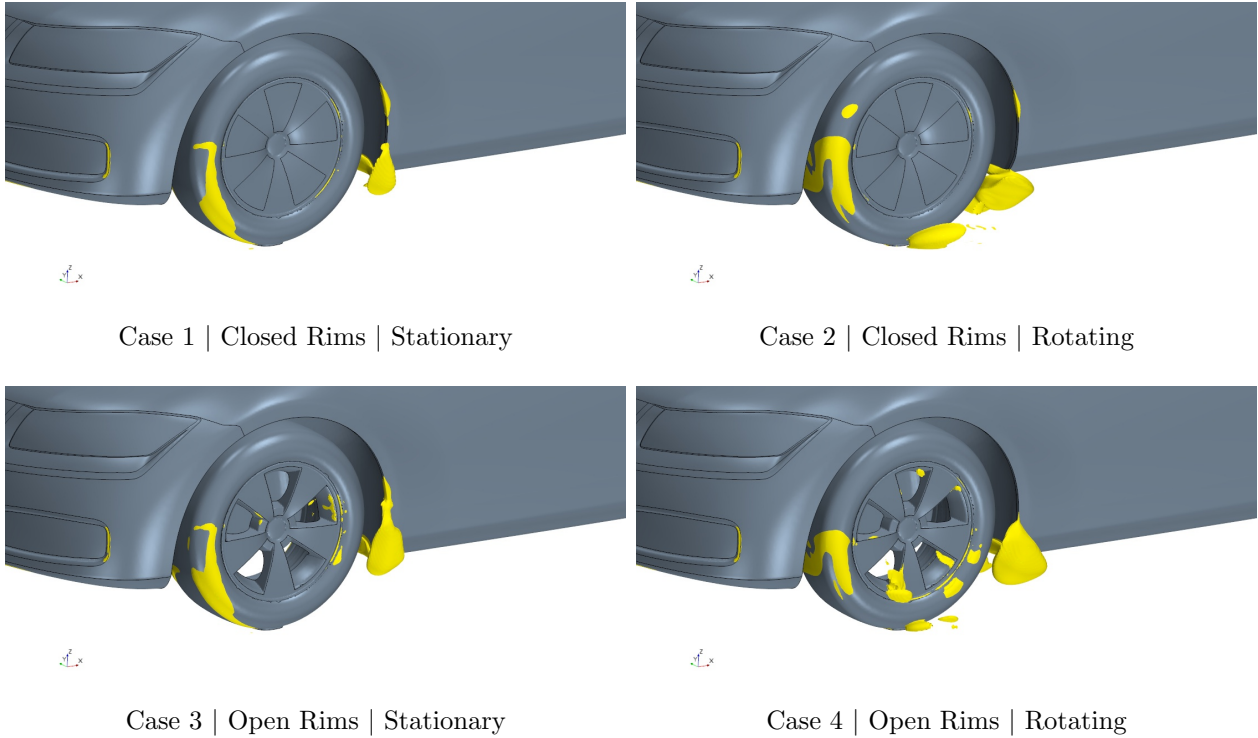


Figure 4.13: Isosurfaces showing Proudman Acoustic Power sound sources at 90 dB.

In Figure 4.14, a cut is presented for the y-plane through the wheels at $y = -850$ mm. The strong source of noise seen in previous figures can be noted right behind the front wheels, and in Case 4 it exceeds 100 dB. It can also be seen at the rear wheels that there is almost no noise above 70 dB in any of the cases, which can be explained by the lower velocities and TKE there.

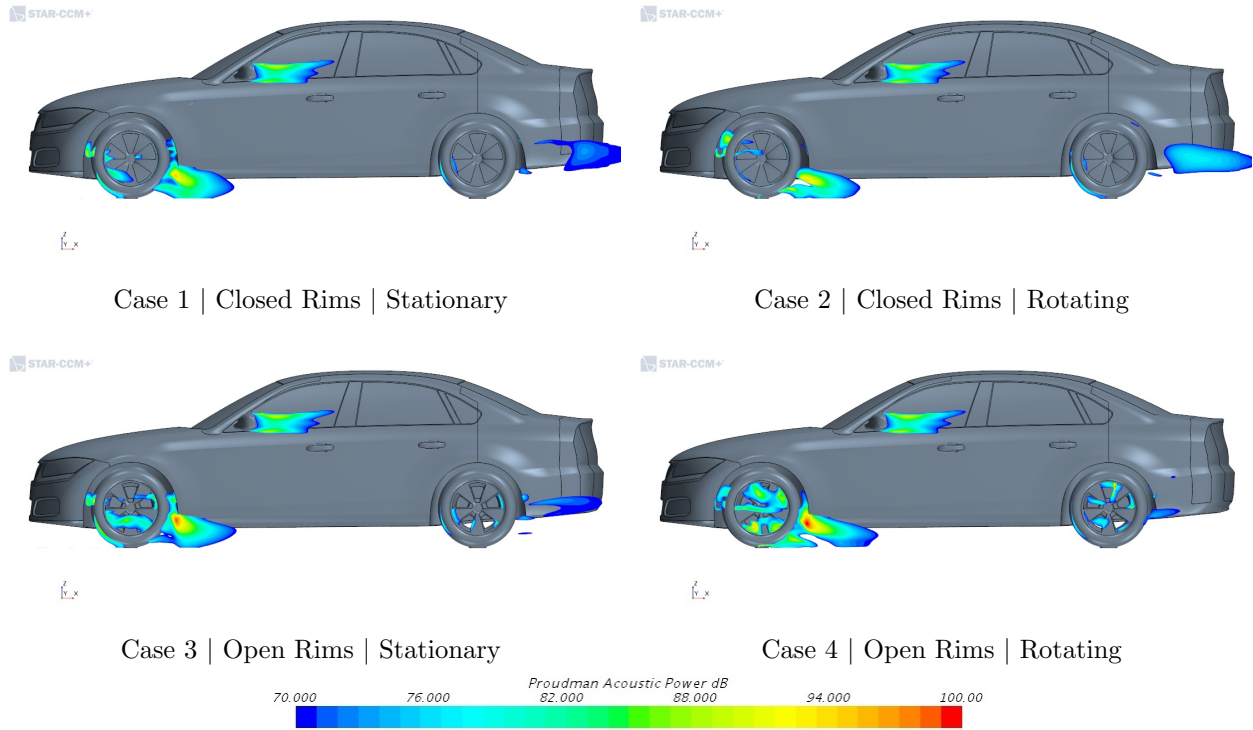


Figure 4.14: A side view cut, through the wheels displaying Proudman Acoustic Power.

4.2.2.1 Proudman Acoustic Power compared to Turbulent Kinetic Energy

In Section 4.2.2 the Proudman sources have been compared to each other. Here, the noise sources are compared to TKE at two levels: 70 and 92 dB. In Figure 4.15 each row symbolizes a case with PAP at 70 dB on the left and TKE at 40 J/kg on the right.

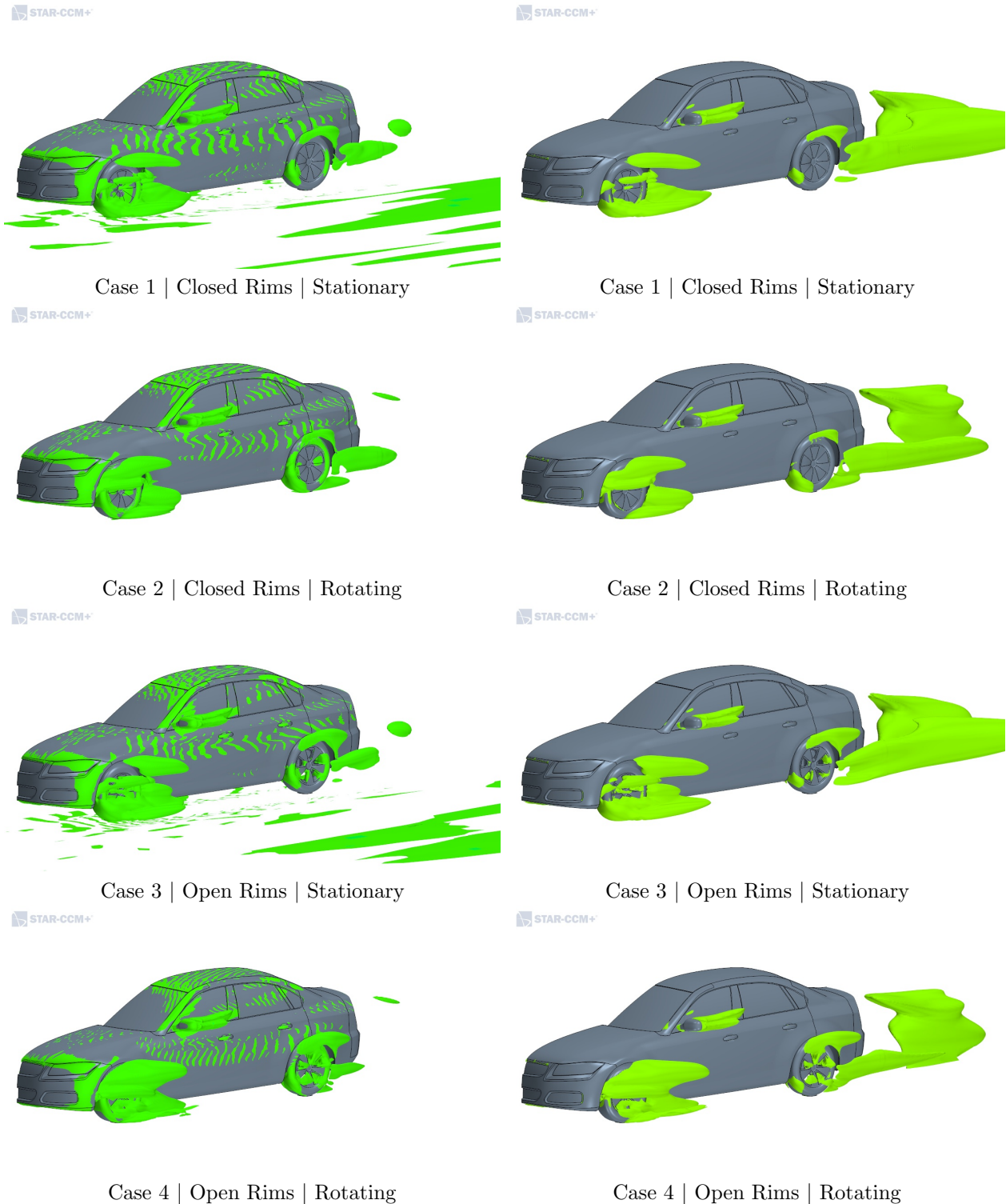


Figure 4.15: Left figures representing isosurfaces of Proudman Acoustic Power at 70dB and the right ones showing isosurfaces of Turbulent Kinetic Energy at 40 J/kg.

At the PAP-level of 70 dB, it can be seen sources of both PAP and TKE at the rear wheel.

The two properties shown are showing striking similarities in size and location, both at the front and the rear. What can be seen is that a significant source of noise can be seen at the rear wheel in Cases 3 and 4 and in Cases 1 and 2 the sources exist but are much smaller.

Also at the much higher decibel level, seen in Figure 4.16 it can be seen that the main sources are at the exact same location. The size and shape is almost identical as well. This can be explained by the Lighthill stress term given in Equation 2.7. It shows that with given conditions it is only dependent on the Reynolds stresses.

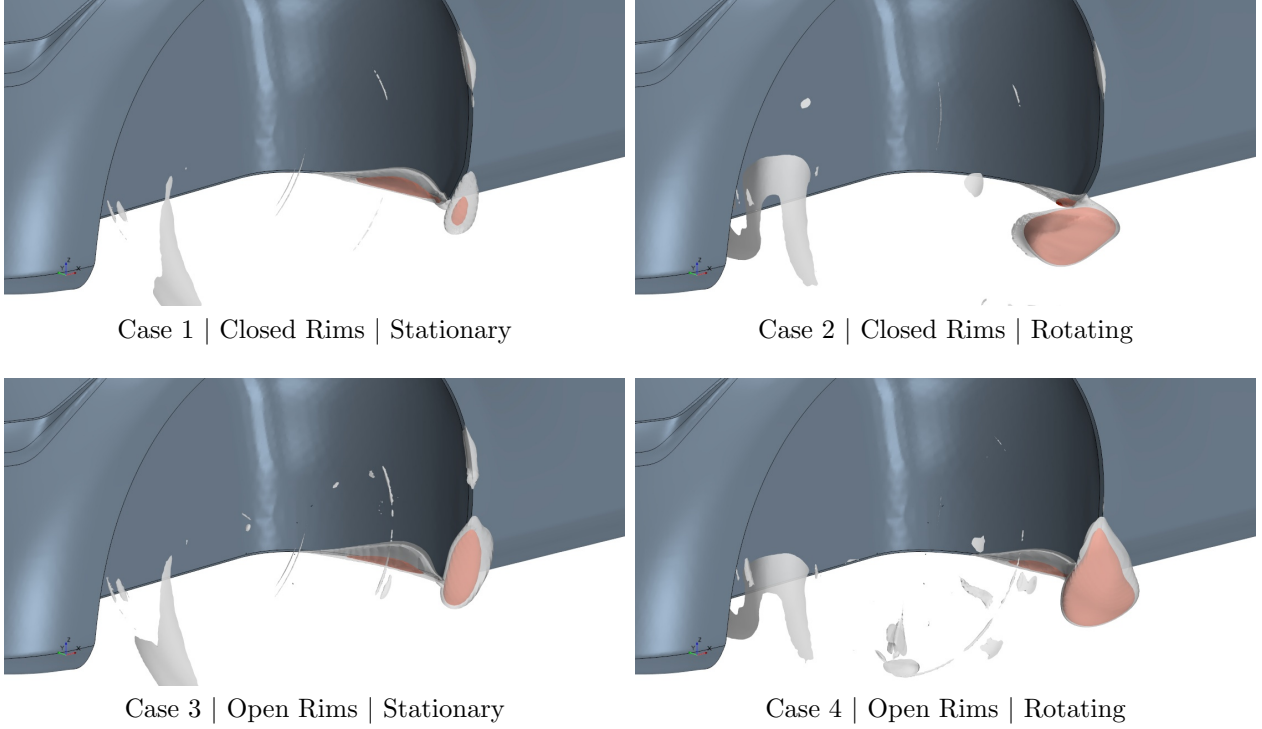


Figure 4.16: A comparison of PAP at 92 dB and TKE at 180 J/kg. PAP represented in grey-scale and TKE in color.

In Table 4.2 the highest magnitudes of PAP obtained are given. The locations can be seen in Figure 4.16 and “Edge” in the table symbolizes the sound source at the edge of the car body behind the front wheel and “Detached” is the noise source shown at the side of the car. It can be seen that in both stationary cases, the edge source is slightly higher than in the rotating cases, but the detached source increases significantly from Case 1 to 2 and slightly from Case 3 to 4. It is assumed that the changed flow characteristics inside the wheel house, when the wheels are set to rotate, is responsible of the change in the sources.

Table 4.2: Maximum Proudman Acoustic Power (dB).

Case	Edge	Detached
Case 1	109	94.5
Case 2	107	100
Case 3	109	98
Case 4	108.5	100

4.2.3 Lilley Noise Source Model

Just like the Proudman model, the Lilley sources are evaluating the effect of quadrupole sources. The Lilley model though, evaluates the turbulent shear flow noise and not the acoustic power.

The model divides the sources into self and shear noise and the combined total is also available to study. In Figure 4.17, a comparison is made between the total and each of the two source terms. As can be seen there, the shear noise term is negligible compared to the self-noise. That can be explained by looking at the equations of the two terms, given in Section 2.2.1.6. The self-noise term consists solely of a product of fluctuation gradients while the shear noise term contains gradients of the mean flow as well. Due to the steady characteristics of the mean flow in the simulations, the terms containing mean flow gradients will by nature be smaller than those containing only turbulent fluctuations.

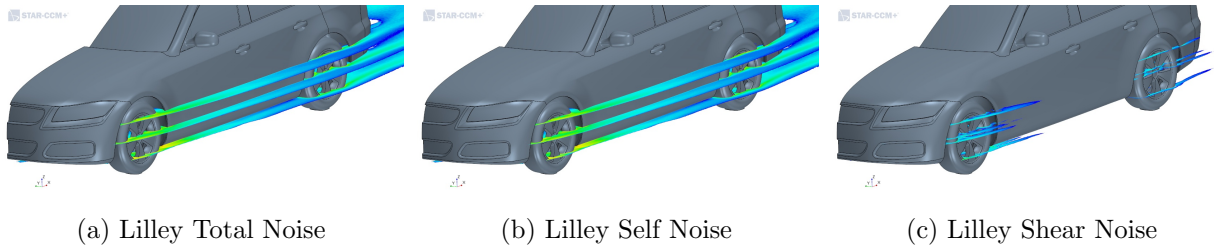


Figure 4.17: A comparison of Lilley Sources a) Lilley Total Noise b) Lilley Self Noise c) Lilley Shear Noise.

Due to the fact that the Lilley sources are in the unit $/s^3$ it felt natural to consider velocity gradients ($/s$), which is done in Figures 4.18 and 4.19. It is clear that stronger sources of noise are found where the velocity gradients are high, although it seems that the velocity gradients persist longer in the flow while the noise tends to decrease faster.

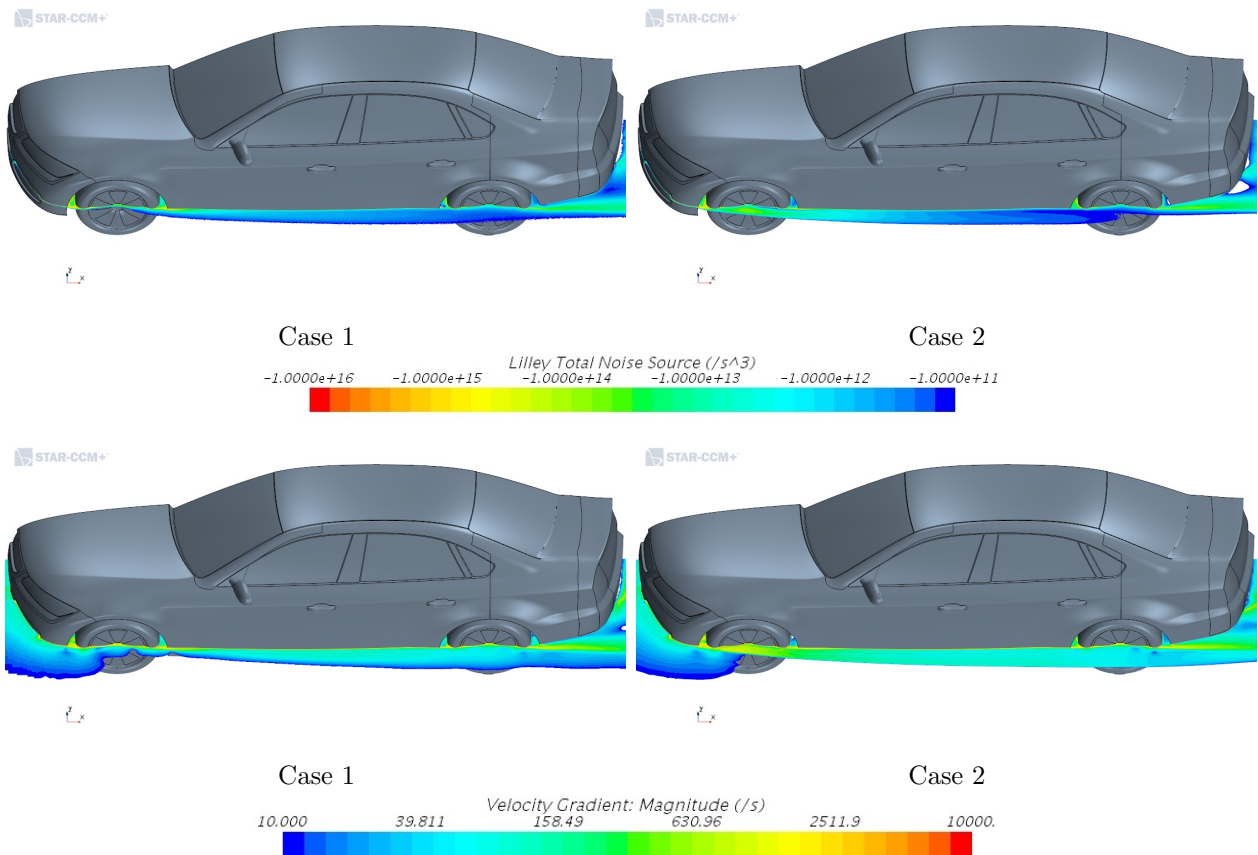


Figure 4.18: A comparison between Lilley Total Noise Sources and velocity gradients on closed rims.

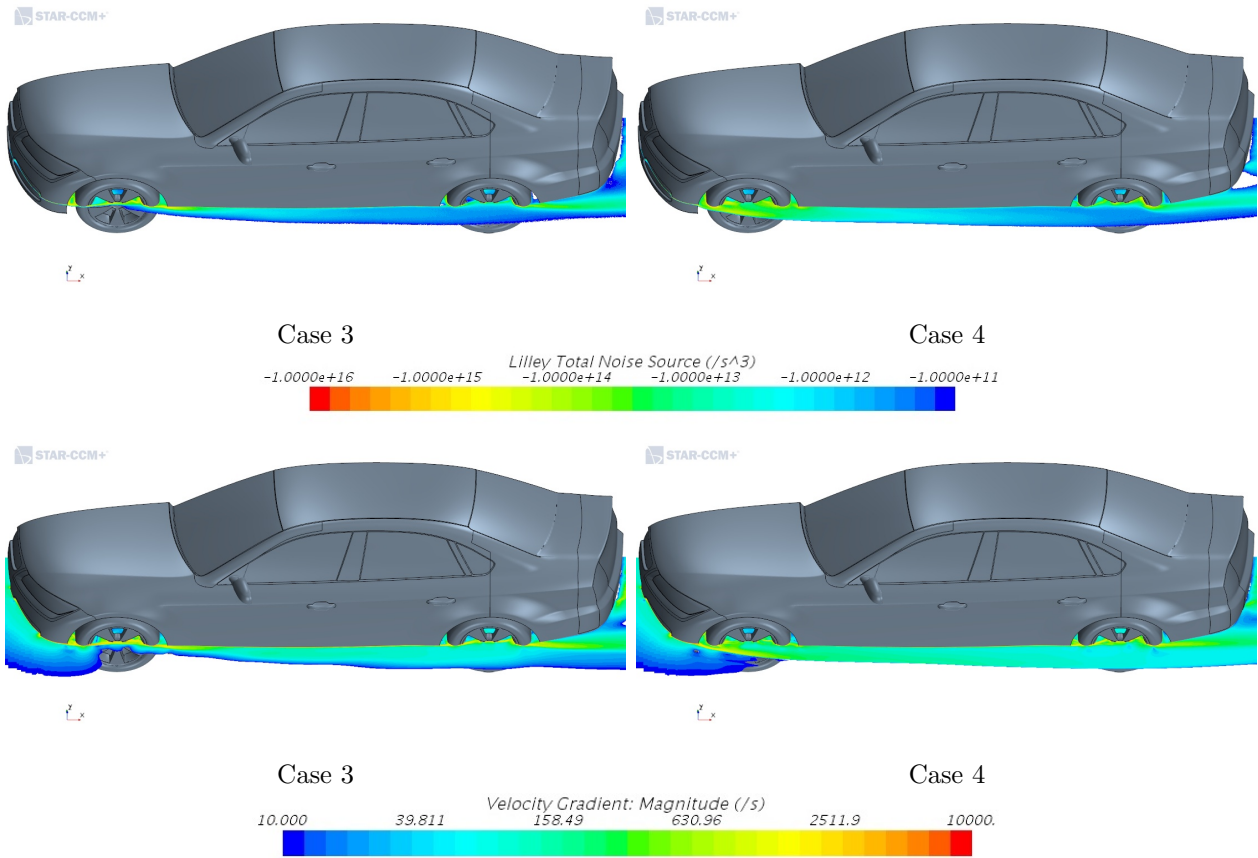


Figure 4.19: A comparison between Lilley Total Noise Sources and velocity gradients on open rims.

5 Conclusions

The study shows that it is essential to find means to reduce the noise generated from the flow around the wheels. All cases studied show significant sources of noise at the front wheels and the simulations have shown a clear dependence of both rim geometry and rotation of the wheels.

When the dipoles on the car surface were studied, using the Curle surface power model, the rim geometry showed no significant contribution to the generated noise, neither in the stationary cases nor in the rotating. The rotation gave, in both geometries, the same increase of approximately 6 dB, at the impingement point of the front wheel.

The Proudman acoustic power model was used to analyze quadrupole sources within the flow, and it was found that the highest intensity found had a much higher dependency on rotation than rim geometry. On the other hand, more intermediate noise was generated from the open rims, and as the measurement is per unit volume, a greater volume generates more noise. The maximum level of acoustic power in both rotating cases is approximately 100 dB while the corresponding values in the stationary cases are closer to 95 and 98 dB.

The final method studied was the Lilley Noise source model where it was found that the shear noise sources were small compared to the internal self-noise sources where only the turbulent fluctuation were considered. A correlation with the velocity gradients of the turbulent flow was found regarding location and intensity.

5.1 Future work

In order to fully understand the generation of the sound sources further studies need to be done on altered geometry, in rim design as well as flow control inside and around the wheel houses. To be able to fully adopt the results of this study, experimental studies should be done and the results need to be compared to the numerical results received here.

Further, the influence from altered geometry of the car should be evaluated to reduce sources of high noise. Other means such as active flow control could be used to evaluate noise reduction. To be able to evaluate the true effect from the noise a transient study should be done with weighted frequency spectra, as humans are more sensitive to certain frequencies than others. Transient simulations need to be done in order to improve methodology. In order to capture instabilities of the flow around the vehicle, a complete car geometry is needed.

Improvements in mesh geometry and simulation settings could be done to improve both simulation time, resources used and the quality of the results. To resolve sufficient frequencies in a transient flow the cell size around the wheels has to be halved.

References

- [1] Council of European Union. *Environmental noise*. http://http://ec.europa.eu/environment/noise/index_en.htm. 2017. (Visited on 05/19/2017).
- [2] European Environment Agency. *EEA 10-2014 Noise in Europe 2014*. <https://www.eea.europa.eu/publications/noise-in-europe-2014>. 2014.
- [3] Council of European Union. *Council regulation (EU) no 540/2014*. <http://eur-lex.europa.eu/legal-content/EN/TXT/PDF/?uri=CELEX:32014R0540&from=EN>. 2014.
- [4] M. Helfer. “General aspects of vehicle aeroacoustics”. *Road Vehicle Aerodynamics*. Ed. by J. Anthoine and L. Löfdahl. Vol. 5. Sint-Genesius-Rode, Belgium: von Karman Institute for Fluid Dynamics, June 2005.
- [5] F. M. White. *Fluid Mechanics*. McGraw Hill, 2009. ISBN: 978-007-127038-0.
- [6] L. Davidsson. *Lecture notes in Mechanics of Fluids*. Mar. 2017.
- [7] D. Moroiianu. “Numerical Simulations of Turbulent Flows at Widely Different Mach Numbers”. PhD thesis. 2005. ISBN: 91-628-6707-5.
- [8] M. J. Lighthill. On Sound Generated Aerodynamically. I. General Theory. *Proceedings of the Royal Society of London. Series A, Mathematical and Physical* **211**.1107 (1952), 564–587.
- [9] N. Curle. The Influence of Solid Boundaries upon Aerodynamic Sound. *Proceedings of the Royal Society of London. Series A, Mathematical and Physical* **231**.1187 (1955), 505–514.
- [10] M. Åbom. *An introduction to Flow Acoustics*. KTH Royal Institute of Technology, Sweden, 2006.
- [11] *STAR-CCM+ User guide*. Version 12.02. <http://steve.cd-adapco.com>. CD-Adapco, 2017.
- [12] I. Proudman. The generation of noise by isotropic turbulence. *Proceedings of the Royal Society of London. Series A, Mathematical and Physical* **214**.1116 (1952), 119–132.
- [13] TU Munich. *DrivAer Model*. <http://www.aer.mw.tum.de/en/research-groups/automotive/drivaer/>. 2017. (Visited on 02/04/2017).
- [14] R. Yazdani. “Steady and Unsteady Numerical Analysis of the DrivAer model”. MA thesis. Chalmers University of Technology, 2015.
- [15] A. Vdovin. “Numerical and Experimental Investigations on Aerodynamic and Thermal Aspects of Rotating Wheels”. PhD thesis. Chalmers University of Technology, 2015.